LOADING CHARACTERISTICS
OF A
CHARGE-CONSTRAINED
SYNCHRONOUS GENERATOR

by

JAMES PETER REGAN

B.E.E., VILLANOVA UNIVERSITY

(1963)

SUBMITTED TO THE DEPARTMENT OF NAVAL ARCHITECTURE AND MARINE ENGINEERING IN PARTIAL FULFILLMENT OF THE REQUIREMENTS OF THE MASTER OF SCIENCE DEGREE IN ELECTRICAL ENGINEERING AND THE PROFESSIONAL DEGREE, NAVAL ENGINEER

at the

MASSACHUSETTS INSTITUTE OF TECHNOLOGY

May, 1968

Signature of Author . . . . . .
Department of Naval Architecture and Marine Engineering, May 17, 1968

Certified by . . . . . .
Thesis Supervisor

Certified by . . . . . .
Reader for the Department

Accepted by . . . . . .
Chairman, Departmental Committee on Graduate Students

LOADING CHARACTERISTICS OF A CHARGE-CONSTRAINED SYNCHRONOUS GENERATOR

BY

JAMES PETER REGAN

ABSTRACT

Submitted to the Department of Naval Architecture and Marine Engineering on May 17, 1968, in partial fulfillment of the requirements for the Master of Science Degree in Electrical Engineering and the Professional Degree, Naval Engineer.

Previous electric-field-type electromechanical energy converters have relied on a variable capacitance, with terminal voltage constrained. An electrostatic generator is studied which employs a spatially varying charge distribution with the potential unconstrained. Energy is converted from mechanical to electrical form by means of a synchronous interaction between the excitation charge wave on the moving medium and the fixed load. Power output characteristics for both a continuum and discrete loading arrangements are derived and analyzed. A study of the effects of discrete loading is essential to understanding operation with a finite number of phases.

It is shown that such generators may be modeled by an equivalent circuit containing a current source in parallel with a characteristic internal capacitance and a load impedance. The values of these circuit elements are determined by the excitation charge wave and geometrical factors such as: load-to-charge wave spacing, charge-to-ground potential distance, and interelectrode spacing and number of phases in the discrete loading case.

For the discretely loaded generator, the output theory is derived by assuming the form of the potential distribution along the loading electrodes. The discreteness requires that Fourier techniques be used and that the distribution be treated as an infinite sum of spatial harmonics of the fundamental wavenumber of the exciting charge wave. A six-phase, discretely loaded generator with an electrode-to-interelectrode width ratio equal to 1.54 is analyzed in detail. It is shown that this generator can deliver 75% of the power available from a continuously loaded generator having the same excitation and physical parameters. Data are presented to predict output power for discrete loadings, with the number of phases varying from five to 42. A six-phase laboratory generator is used to determine the equivalent circuit element values.

The theory predicts the current source magnitude to within 6%. With the stray capacitance due to electrode structure quantified and included, the characteristic internal capacitance is predicted to within 5% by the theory.

Thesis Supervisor: James R. Melcher
Title: Associate Professor of Electrical Engineering

ACKNOWLEDGEMENTS

The author wishes to express his appreciation to all those who helped to make the completion of this thesis possible. He especially thanks Professor James R. Melcher for suggesting this problem and for guidance and assistance at all stages of the research.

The author particularly appreciates the assistance of Mr. Edmund B. Devitt, who checked calculations throughout the preparation. He also wishes to thank Mrs. Evelyn Homes for her efficient typing of this manuscript, and Mr. Harold Atlas, who provided invaluable assistance in the construction of the laboratory apparatus.

Grateful thanks are also due my wife, Janet, for her patience and understanding.

Financial support for this research was provided by the National Aeronautics and Space Administration and the United States Navy.

LIST OF FIGURES

(List of Figures continued)

TABLE OF CONTENTS

CHAPTER I

INTRODUCTION AND BACKGROUND

The past several decades have seen the development of electromechanical energy conversion machinery which has provided our industrial societies with a means for rapid technological growth. The scientists who experimented with electrical phenomena a century ago would not have predicted the posture of electricity in today's world, even in their most optimistic dreams. Since its implementation, electrical power has become an integral part of man's daily activity.

The dependence of modern society on electric machinery is due to strong economic factors. Kinetic energy from a natural water fall may be converted cheaply and efficiently to electrical energy and then transmitted, with small loss, over great distances to industrial and population centers so as to provide useful work.

With relatively few exceptions, magnetic fields serve as the energy coupling mechanism for modern electromechanical energy conversion equipment. Until recently, the development of electric-field-based energy conversion machinery as a practical source of significant amounts of electrical power has received only passing interest. Historically, electric-field energy conversion devices were of great interest to those most intently involved in the development of electrical science during the nineteenth century. These machines were for the most part direct current generators with an energy storage capability, and were employed principally as experimental laboratory apparatus.[9] The twentieth century thus far has seen the Van de Graaff high-voltage direct current generator as probably the most significant development in electric-field energy conversion machinery.

The lack of development of electric-field machinery for power production has been due largely to severe limitations imposed by electric field breakdown strength at atmospheric pressure. Magnetic field systems are not limited by a breakdown phenomenon, and by employing them as the coupling medium, energy densities can be attained which are much greater than those attainable with electric fields before breakdown.

With the magnitudes of the electric and magnetic field energy densities as a direct measure of their capacity to deliver power, a comparison of the two types of machinery as energy converters may be readily accomplished[3]

Magnetic field energy density: $E_B = \frac{1}{2}\frac{B^2}{\mu}$ joules/m^3

Electric field energy density: $E_E = \frac{1}{2}\varepsilon E^2$ joules/m^3

Now, to compare the two energy densities, consider

$$\eta = E_B/E_E$$

To evaluate this ratio it is necessary to assign magnitudes to the magnetic and electric field intensities. For field strengths normally attainable without the use of coolants or vacuum systems, we have:

$$B \cong 1 \text{ weber/m}^2$$

$$E \cong 3 \times 10^6 \text{ volts/m}$$

Using these values and recalling that for atmospheric air

$$\mu \cong 4\pi \times 10^{-7} \text{ weber/amp-turn m}$$

and

$$\varepsilon \cong 8.854 \times 10^{-12} \text{ farad/m}$$

the relative energy density ratio may be evaluated:

$$\eta \cong 10^4$$

This calculation has exposed the advantage which has propelled magnetic field equipment into its present monopolistic position among low-frequency electromechanical energy conversion machinery.

However, modern technology has made available high vacuum systems and techniques for efficiently employing them which promote a questioning attitude toward the efficacy of the above energy density comparison. In a high-vacuum environment, it has been demonstrated[7] that an improvement by a factor of 30 in electric field breakdown strength is not out of reach.

In light of this information it is important to ask the question, "If given a very large electric field energy density, can it be practically employed in a generator as the coupling medium for power production?" It is with the objective of answering this question, at least partially, that this paper is being prepared.

The impetus for the research was provided by the recent work done investigating electrofluid-dynamic (EFD) power sources, conducted by the Continuum Electromechanics Group here at M.I.T. In turn, the need for such equipment has been supplied by the space industry and their applications for light-weight electric power generators aboard space vehicles. Electric-field-based generators offer a distinct advantage in power delivered per unit weight over their magnetic field counterparts.

An EFD generator, characterized by a high voltage, low current output, was proposed and constructed as the subject of two recent M.I.T. Theses[10,11]. The scheme employed a high velocity air flow with entrained particles which were sinusoidally charged in a corona exciter. The flow, a traveling wave of charge, passed from the exciter through a long, slender channel surrounded

by a conducting medium. The charge wave interacted synchronously with the conductor, converting kinetic energy from the particle flow into electric energy which was dissipated as heat. The energy conversion interaction used in this generator is the electric field analogue of the interaction which converts kinetic energy to electric energy for magnetic field synchronous machines.

The synchronous electric field generator proposed and built during the research for this paper resulted from an attempt to model the charged particle flow realized in the EFD generator in order that loading characteristics could be studied. Details of the generator built are set forth in Appendix B. A standing wave of charge density on a rotating disk was used to approximate a traveling charge wave passing through a long slender channel. Synchronism was obtained by establishing an integral number of wavelengths of charge distribution around the disk periphery.

Other attempts to build electric field synchronous generators are not unknown.(7) However, these have been voltage-constrained machines depending on a spatial rate of change of capacitance to provide the mechanism for energy conversion. These types of synchronous machines are the electric field analogue of the synchronous reluctance machinery in the magnetic field system. The EFD generator discussed and the one built for this thesis research are charge-constrained synchronous generators requiring a spatial gradient in the exciting charge density, and no spatial capacitance gradient, for energy conversion. The magnetic field analogue for this machine is what is known simply as a 'smooth-air-gap synchronous generator'.

It is interesting to note some of the salient advantages that the charge-

constrained machine possesses over the voltage-constrained machine. The electrode blade structure in the voltage-constrained machine undergoes very rapidly alternating electric pressure forces which present designers with the possibility of an instability occurring in one of several possible modes of vibration. The severity of this problem is obvious when the blade spacing is of the order of a millimeter and the rotational speeds approach 30,000 RPM. The torque-time history for such a machine shows rapid fluctuations due to the time-varying electric traction as the blades move in and out of each other's influence. Both of these problems impose severe limitations on the feasibility of high rotational velocity operation, which is essential to the production of large amounts of power.

In contrast, the charge-constrained synchronous generator does not require a spatial gradient in capacitance, hence removes these limitations on the feasibility of high speed operation. For this machine, the electrical traction force on each part of the rotor (and therefore the mechanical torque) is constant in time. Also, the severity of the alternating pressure forces acting on the electrode structure is greatly diminished with several electrodes per wavelength of induced voltage. For continuous loading, as is discussed in Chapter II, this effect is even further reduced.

In summary, this research concerns itself with a charge-constrained synchronous generator placing particular emphasis on providing a theory by which the output of such a generator might be predicted from its physical parameters and charge wave description. An actual generator was built to allow for a direct comparison of theory and experiment. Through this comparison, it is hoped that a step forward in the development of a new scheme for the generation of electrical power has been made.

CHAPTER II

CONTINUOUS LOADING

Introduction:

A detailed analysis of the continuously loaded, charge-constrained synchronous generator can provide an excellent insight into the energy conversion interaction involved. This development will serve as the basis for subsequent analysis in Chapter III of the discretely loaded generator. The geometry of the continuously loaded generator will be modeled as shown in Figure 2.1. The excitation source for this generator is a sheet of sinusoidally distributed surface charge density traveling along the channel centerline at a fixed velocity. To an observer fixed in the frame of the load, this would appear as a traveling wave of charge. The power output of the generator will be measureable in terms of resistive heating in the conducting load. In this chapter, the source and load will be reduced to lumped circuit elements normalized to channel load interfacial area. This equivalent circuit approach will prove to be a powerful technique for studying such a generator and will be extended to the discretely loaded case in Chapter III.

Governing Equations:

From Fig. 2.1, this problem involves two distinct regions, the load and the channel. The most direct method for determination of the fields is to assume a potential distribution at the load-channel interface, solve the bulk equations independently in each region, and then match solutions at the interface. Because of the symmetry of the problem about the $y = 0$ axis, it is apparent that the problem need be solved only for the upper region, with solutions for the lower region taking the same form.

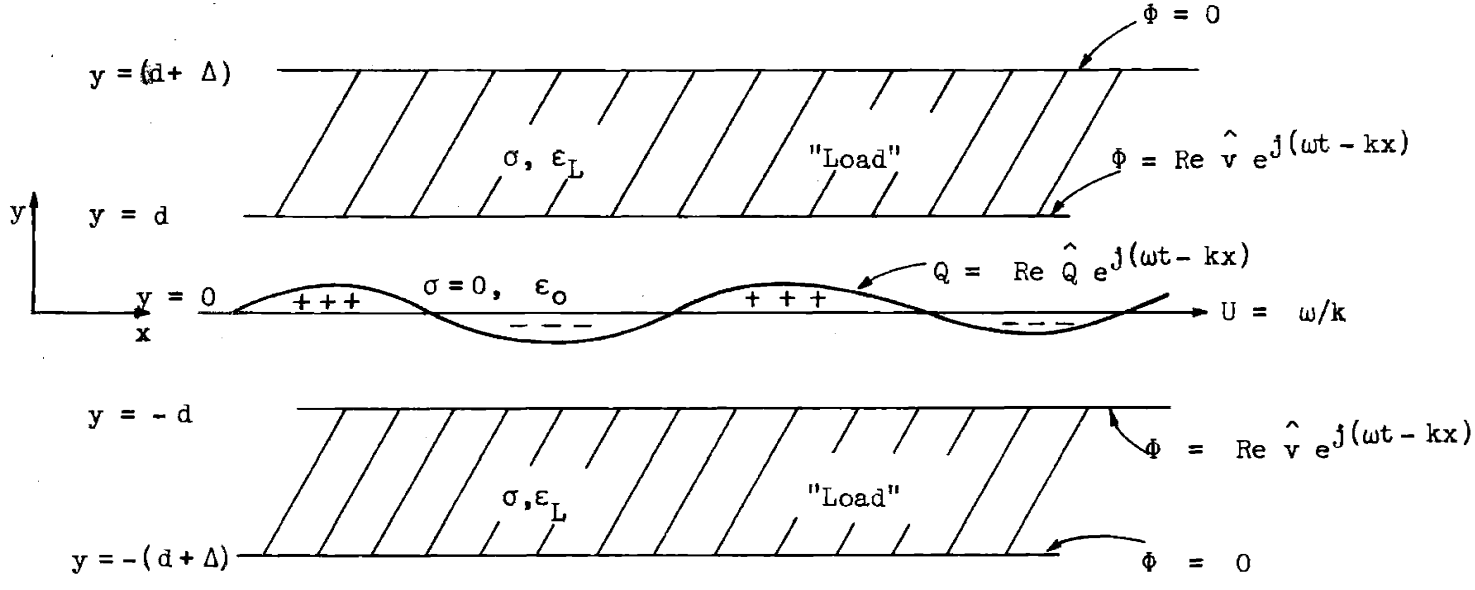

Figure 2.1

Continuously Loaded Generator

From Maxwell's equation, the governing equations for the two regions of interest are:

$$\begin{aligned} &\text{(a) Region (1)} \quad \nabla^2\phi_C = 0 \qquad 0 \le y \le d \\ &\text{(b) Region (2)} \quad \nabla^2\phi_L = 0 \qquad d \le y \le d + \Delta \end{aligned} \tag{2.1}$$

Since the potentials in both regions are established due to the influence of the traveling wave of charge, they will be assumed to be traveling waves in form also, with the same wavenumber as the charge wave. Potential variations in the z direction may be neglected, as the channel is assumed slender and wide such that $2d/W \ll 1$. On this basis, the potential distributions must take the form:

$$\phi = \text{Re}\ \hat{\phi}(y)\ e^{j(\omega t - kx)} \tag{2.2}$$

Substitution of the assumed form of the potential solution (Eq. 2.2) into the governing equations (2.1) yields for each region:

$$\frac{d^2\hat{\phi}(y)}{dy^2} - k^2\hat{\phi}(y) = 0 \tag{2.3}$$

The potential solutions therefore are:

$$\begin{aligned} &\text{(a)} \quad \hat{\phi}_C(y) = A_C \cosh ky + B_C \sinh ky \qquad 0 \le y \le d \\ &\text{(b)} \quad \hat{\phi}_L(y) = A_L \cosh ky + B_L \sinh ky \qquad d \le y \le d + \Delta \end{aligned} \tag{2.4}$$

Boundary Conditions:

Evaluation of the four constants in equation (2.4) will complete the determination of the potential distribution. This requires four independent

boundary conditions on the fields. By specifying an assumed potential distribution along the interface as indicated on Fig. 2.1, and by specifying the location of zero potential at the outer boundary of the conductor, three boundary conditions are available:

$$\begin{aligned} &(a) \qquad \hat{\phi}_C(y=d) = \hat{V} \\ &(b) \qquad \hat{\phi}_L(y=d) = \hat{V} \\ &(c) \qquad \hat{\phi}_L(y=d+\Delta) = 0 \end{aligned} \tag{2.5}$$

The last boundary condition is obtained from the charge sheet. At the sheet, the normal component of the electric field is equal to one-half the magnitude of the charge density divided by the dielectric constant. The factor of one-half is due to the symmetry of the channel; half of the charge excites the upper region and half excites the lower region. This boundary condition becomes:

$$(d) \qquad \left.\frac{d\hat{\phi}_C(y)}{dy}\right)_{y=0} = -\frac{1}{2\varepsilon_o}\hat{Q}$$

Solutions:

Applying the boundary conditions of equation (2.5) to potential solutions expressed in equation (2.4) leads to the following matrix equation for the unknown constants.

$$\begin{bmatrix} \cosh kd & \sinh kd & 0 & 0 \\ 0 & 1 & 0 & 0 \\ 0 & 0 & \cosh k\Delta & \sinh k\Delta \\ 0 & 0 & 1 & 0 \end{bmatrix} \begin{bmatrix} A_C \\ B_C \\ A_L \\ B_L \end{bmatrix} = \begin{bmatrix} \hat{V} \\ -\hat{Q}/2\varepsilon_o k \\ 0 \\ \hat{V} \end{bmatrix} \tag{2.6}$$

Evaluation of the constants and substitution into Equation (2.4) completely specifies the fields in terms of the charge density and the assumed potential distribution on the interface.

$$\text{(a)}\quad \hat{\phi}_C(y) = \left[\frac{\hat{V}}{\cosh kd} + \frac{\hat{Q}}{2\varepsilon_o k}\tanh kd\right]\cosh ky - \frac{\hat{Q}}{2\varepsilon_o k}\sinh ky$$

$$\text{(b)}\quad \hat{\phi}_L(y) = \hat{V}\cosh k(y-d) - \hat{V}\coth k\Delta \sinh k\,(y-d) \qquad (2.7)$$

Equivalent Circuit:

Using equation (2.7) it is now possible to develop an equivalent circuit which characterizes the channel and load interaction. First the load is characterized by calculating the total current density, conduction current plus displacement current, which flows into the load region normal to the interface as a function of the assumed potential distribution. This load current density is a traveling wave with the same wavenumber as that of the potential and its complex amplitude is given by:

$$\text{(a)}\quad \hat{J}_{Ly}\Big)_{y=d} = \sigma\hat{E}_y\Big)_{y=d} + \frac{\partial \hat{D}_y}{\partial t}\Big)_{y=d} \qquad (2.8)$$

In terms of the potential distribution of equation (2.7 b),

$$\text{(b)}\quad \hat{J}_{Ly}\Big)_{y=d} = \sigma\left[-\frac{d}{dy}\hat{\phi}_L(y)\right]_{y=d} + j\omega\varepsilon_L\left[-\frac{d}{dt}\hat{\phi}_L(y)\right]_{y=d}$$

Performing this calculation and defining equivalent circuit elements completely characterizes the load region.

$$\hat{J}_L = [j\omega C_L + G_L]\hat{V} \quad \text{amps/m}^2 \ y=d \qquad (2.9)$$

where:

$$\text{(a)}\quad C_L = k\varepsilon_L \coth k\Delta \ \text{farads/m}^2 \qquad (2.10)$$

$$\text{(b)}\quad G_L = \sigma k \coth k\Delta \ \text{mhos/m}^2$$

The channel may now be characterized in a manner similar to that used for the load to obtain the current density normal to the interface out of the channel region.

$$\hat{J}_C = [- j\omega C_C \hat{V} + \hat{J}_S] \text{ amps/m}^2 \qquad y=d \tag{2.11}$$

where an equivalent capacitance and source have been defined.

$$\begin{aligned} &\text{(a)} \quad C_C = k\varepsilon_o \tanh kd \quad \text{farads/m}^2 \\ &\text{(b)} \quad \hat{J}_S = \frac{j\omega \hat{Q}}{2 \cosh kd} \quad \text{amps/m}^2 \end{aligned} \tag{2.12}$$

The equivalent circuit may now be obtained by recognizing that there is no time rate of free surface charge at the interface, and therefore the current densities out of and into the interface,as represented by equations (2.9) and (2.11) respectively,must be equal.

$$[\, j\omega C_L + G_L]\hat{V} = - j\omega\, C_C \hat{V} + \hat{J}_S \tag{2.13}$$

The equivalent circuit for the generator which represents the load-channel interface as a terminal pair is shown below in Figure 2.2.

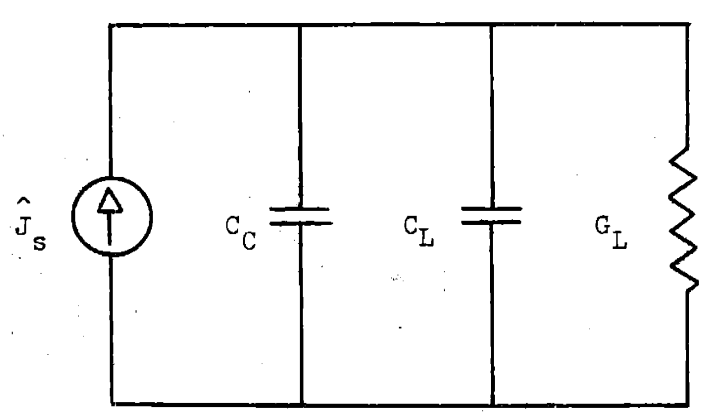

Figure 2.2

Power Output Calculation:

The computation of the time average power delivered to the load on a per square meter of channel-load interfacial area basis is straightforward, making use of the equivalent circuit of Figure (2.2). The power output found in this way is the power delivered to the upper load region only; it is multiplied by two to account for the lower load. The total power output is:

$$\langle P \rangle = \mathrm{Re}\left[\frac{\hat{J}\,\hat{J}^*}{G_L}\right] \quad \text{watts/m}^2 \tag{2.14}$$

In terms of known quantities:

$$\hat{J} = \frac{G_L\,\hat{J}_S}{j\omega[C_C + C_L] + G_L} \quad \text{amps/m}^2 \tag{2.15}$$

therefore:

$$\langle P \rangle = \frac{G_L\,|\hat{J}_S|^2}{G_L^2 + \omega^2[C_C + C_L]^2} \quad \text{watts/m}^2 \tag{2.16}$$

Power Optimization:

The power output expression of equation (2.16) can be plotted as a function of load conductance for fixed channel and load geometry and fixed charge flow condition.

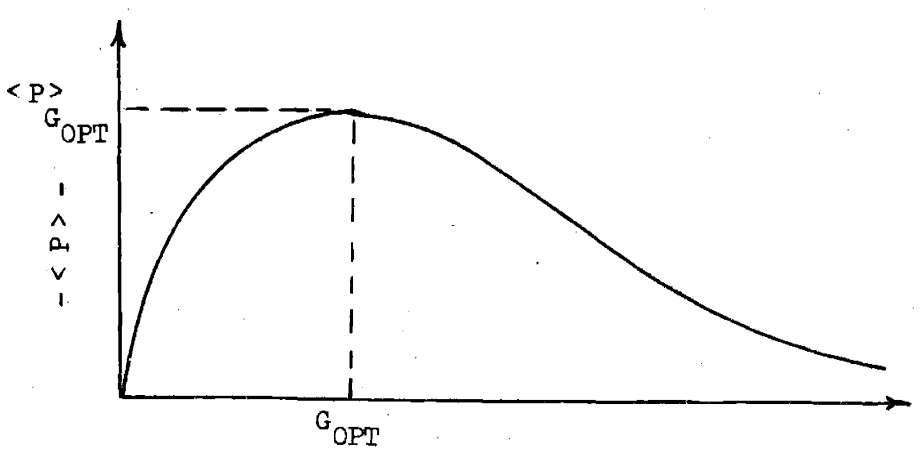

Fig. 2.3

From Fig. 2.2, it is obvious that there exists some optimum conductance G_{OPT} for which the maximum amount of power is delivered across the interface to the load. To locate this optimum, maximize Equation (2.16) over G_L:

$$\frac{\partial \langle P \rangle}{\partial G_L} = 0 \tag{2.17}$$

Carrying out the calculation specified by Equation (2.17) yields:

$$G_{OPT} = \omega[C_C + C_L] \text{ mhos/m}^2 \tag{2.18}$$

The optimum power is obtained by substitution of Eq. (2.18) into (2.16):

$$\langle P \rangle_{G_{OPT}} = \frac{\omega \, |\hat{Q}|^2}{8[C_C + C_L]\cosh^2 kd} \text{ watts/m}^2 \tag{2.19}$$

It is important to note that Eq. (2.19) is only a limited optimization. In general,

$$\langle P \rangle = f\,(\hat{Q}, \omega, \sigma, d, \Delta, \varepsilon_o, \varepsilon_L, k) \tag{2.20}$$

This function may be considered as an eight-dimensional vector which traces some complex surface as the values of the independent variables are ranged. The absolute optimum power can be found only be considering all eight variables. The preceding optimization ranged but one variable -- conductivity.

Another important factor to take into account when optimizing is the electric field breakdown strength.[5] It will determine whether or not an optimum point is indeed physically realizable.

CHAPTER III

DISCRETE LOADING

Introduction:

The continuously loaded, charge-constrained synchronous generator analyzed in Chapter II provided a simple mathematical model which placed particular emphasis on the salient features of generator operation. In terms of this model, the fundamental energy conversion interaction may be readily understood. However, as a practical matter, a generator of this type is of very limited value for use as a source of electrical power. Most equipment requiring electrical power for operation has discrete electrical terminals, and cannot be considered as a continuous type of load. Therefore, of more direct interest in determining the feasibility for power production would be an analysis of a discretely loaded generator. Rather than an infinite continuous loading, there would be discrete electrodes of finite width used to tap off the electrical power, which could then be transmitted to the locations where electrical machinery and/or equipment are employed. The number of phases would be determined by the number of electrodes per wavelength of exciting charge wave.

An analysis of such a generator will be presented in this chapter, using the techniques developed in Chapter II for obtaining an equivalent circuit. The physical characteristics of the generator under discussion are as shown in Figure 3.1.

Voltage Distribution Model:

As in the case of a continuum load, it is necessary to solve a two-region problem governed by Laplace's equation. The principal difference between the continuum and discrete loading cases is in the form of the

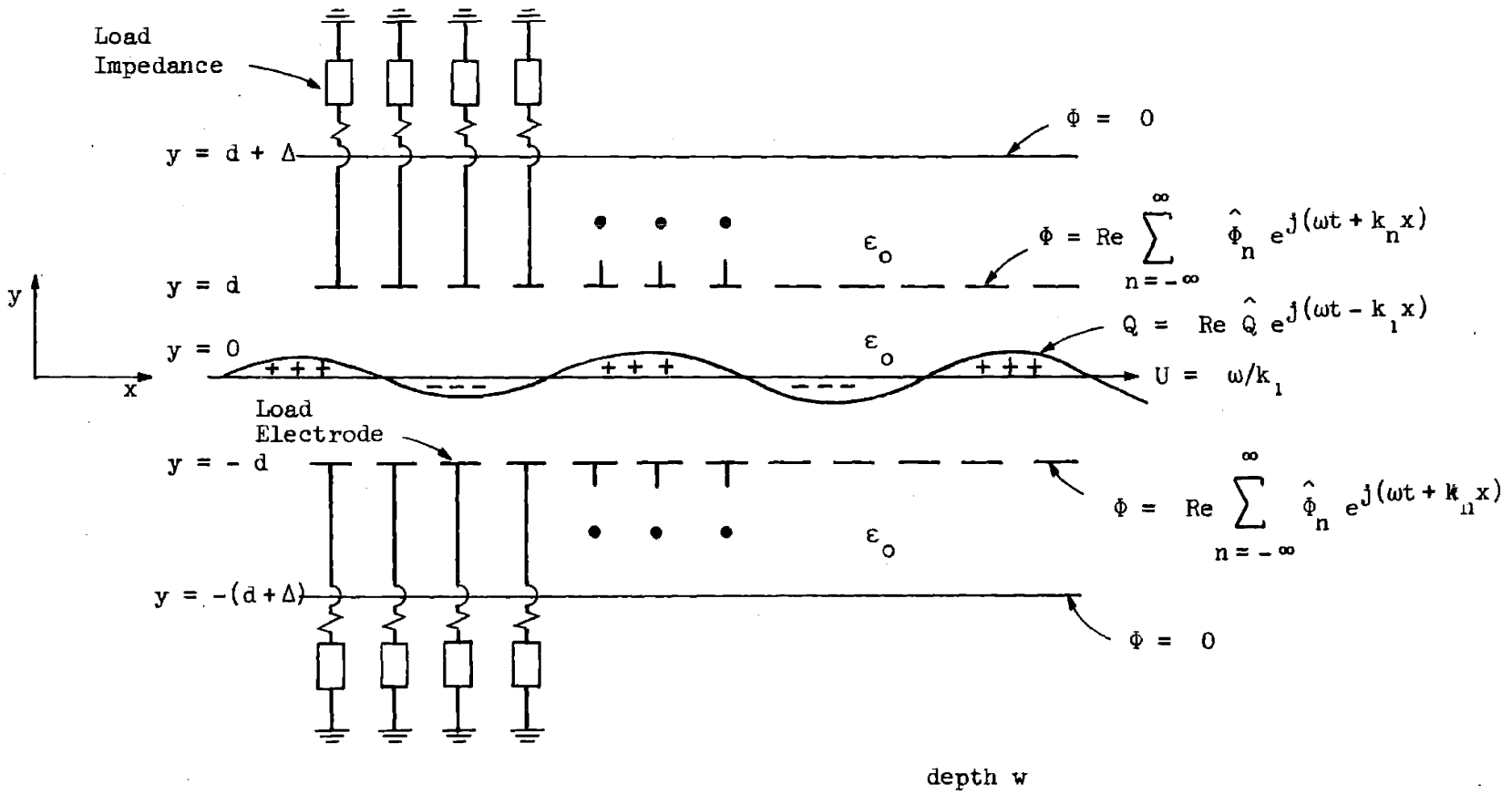

Figure 3.1

Discretely Loaded Generator

potential distribution along the electrodes on the channel boundary. Due to the finite electrode structure, it is incorrect to assume a potential wave with the same wavenumber as the exciting charge wave. Rather, spatial harmonics of the fundamental wavenumber are introduced and the potential distribution takes the form of a sum of an infinite series of traveling waves. This allows the problem to be analyzed by means of Fourier techniques.

In order to proceed with a Fourier analysis, it is necessary to obtain a model for the potential distribution along the channel electrodes. The first and most obvious constraint on this distribution model is that the potential across each electrode must be a constant, since they are assumed to be perfect conductors. To determine the potential distribution between adjacent electrodes, to be used in the model, two possible courses of action present themselves. The first is to specify that there is zero net current density flow normal to the channel axis into the load channel interface. That is to say, there is no time rate of change of free charge on the interface in the interelectrode regions. The second course of action is to assume the form of the potential distribution between electrodes, based on physical reasoning.

With the electrode spacing assumed to be small compared to a wavelength of the exciting charge wave, a linear potential distribution between electrodes is felt to be a good approximation, and therefore the second course of action will be followed in the ensuing analysis. It is acknowledged that the first alternative would provide a more exact solution; however, the increased complexity of the problem would serve only to confuse, rather than

to expose the basic principles involved in discrete loading. It will be shown in Chapter IV that the results predicted by this model are reasonably close to those realized from an actual generator. It should be noted here that the slope of the assumed linear distribution must be kept finite, as an infinite slope such as would result from a stepped potential distribution implies an infinite capacitance. Fortunately, as will become clear in the analysis, the capacitance is not a strong function of slope.

Now that the general form of the potential distribution model has been determined, the pieces must be put together in such a way as to maintain the identity of each electrode in the solution. This is desirable, since, when using the generator, each electrode's output must be determinable in terms of its own loading and that of each of the other electrodes. This may be accomplished by isolating all electrodes of the same phase as a periodic potential distribution in space, which can then be Fourier-analyzed independently of the electrodes contained in the other phases. The total potential distribution in space can then be obtained by summing these Fourier series over the number of phases per fundamental wavelength. The identity of each phase is maintained by assigning to it an index. The time frequency of each Fourier component in this analysis will be identical to the time frequency of the charge distribution wave.

Consider the case where there are s electrodes per fundamental wavelength, then the potential distribution associated with the r'th electrode phase will be assumed to be of the following form:

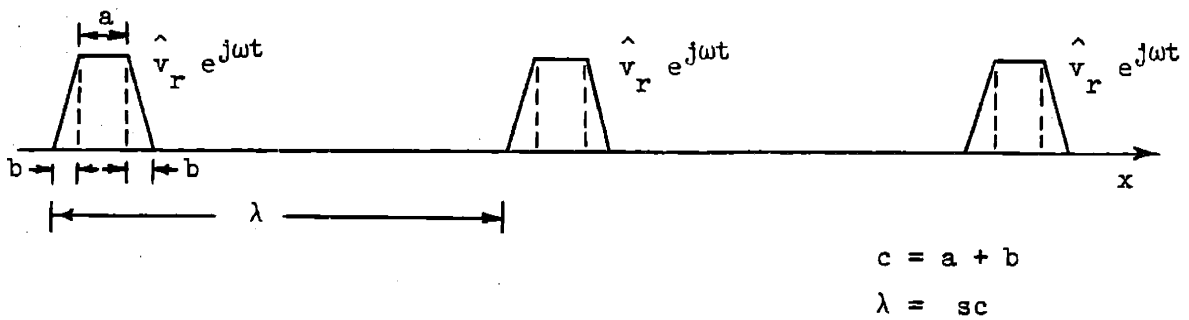

Figure 3.2

$$\hat{v}_r(x) = \begin{cases} V_{r/b}[x-(r-1)c] & (r-1)c \le x \le (r-1)c+b \\ V_r & (r-1)c+b \le x \le rc \\ V_{r/b}[b-x+rc] & rc \le x \le rc+b \end{cases} \tag{3.1}$$

A wavelength of potential distribution for the case of six (6) electrodes per wavelength would then have the following form.

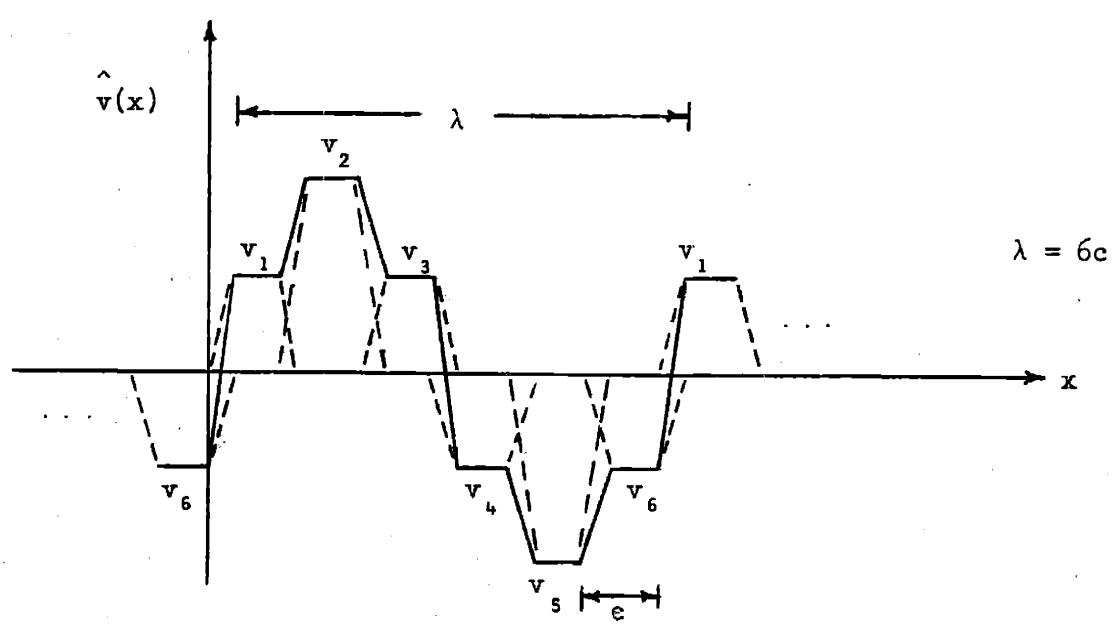

Figure 3.3

Fourier Analysis:

In terms of the preceding discussion, the potential distribution on the electrodes may be expressed as

$$v(x,t) = \mathrm{Re} \sum_{r=1}^{s} \hat{v}_r(x) e^{j\omega t} \tag{3.2}$$

The complex amplitudes are determined from the infinite sum.

$$\hat{v}_r(x) = \frac{1}{sc} \sum_{n=-\infty}^{\infty} \hat{v}_{r_n} e^{jk_n x} \tag{3.3}$$

where

$$k_n = \frac{2\pi n}{sc} \tag{3.4}$$

The Fourier coefficients for the series (3.3) are obtained from the following sum of integrals using Equation (3.1).

$$\hat{v}_{r_n} = \int_{(r-1)c}^{(r-1)c+b} \frac{V_r}{b} [x-(r-1)c] e^{-jk_n x} dx + \int_{(r-1)c+b}^{rc} V_r e^{-jk_n x} dx + \int_{rc}^{rc+b} \frac{V_r}{b} [b - x + rc] e^{-jk_n x} dx \tag{3.5}$$

Performing the above-indicated integrations yields the following Fourier coefficients for the r'th electrode:

$$\hat{v}_{r_n} = \frac{V_r e^{-jk_n rc}}{b k_n^2} \left[4 e^{\frac{jk_n a}{2}} \sin \frac{k_n c}{2} \sin \frac{k_n b}{2} \right] \tag{3.6}$$

Using this result together with Equations (3.2) and (3.3) completely specifies the complex amplitude of the potential distribution along the electrodes in terms of the assumed model and its phase amplitudes.

$$\hat{v}(x) = \sum_{r=1}^{s} \sum_{n=-\infty}^{\infty} \frac{V_r e^{-jk_n rc}}{scb\ k_n^2} \left[4e^{\frac{jk_n a}{2}} \sin\frac{k_n c}{2} \sin\frac{k_n b}{2} \right] e^{jk_n x} \tag{3.7}$$

This completes the Fourier analysis and provides the basis for characterizing the generator by an equivalent circuit.

Governing Equations:

From Fig. 3.1 the symmetry of the generator channel about its centerline is apparent. It is therefore only necessary to solve the fields problem in the upper channel and load region, since the lower solution must take the same form. The governing equations for the two regions are the same, as in the case of continuous loading.

$$\begin{aligned} &(a) \quad \nabla^2 \Phi_C = 0 \qquad && 0 \leq y \leq d \\ &(b) \quad \nabla^2 \Phi_L = 0 \qquad && d \leq y \leq d + \Delta \end{aligned} \tag{3.8}$$

In the preceding section the potential distribution along the load electrodes was analyzed as an infinite sum of harmonically related traveling waves. Since the potential in both the channel and load regions must equal the assumed distribution at the interface, it is efficient to think of the potential distribution in these regions as also being made up of an infinite sum of traveling waves, harmonically related to the exciting charge wave. Each of these harmonics will therefore be required to satisfy equation (3.8) independently. That is to say, for both regions of interest the potential wave will be of the form:

$$\Phi(x,y,t) = \mathrm{Re} \sum_{n=-\infty}^{\infty} \hat{\Phi}_n (x,y,t) \tag{3.9}$$

where

$$\hat{\Phi}_n(x,y,t) = \hat{\Phi}_n(y)\, e^{j(\omega t + k_n x)} \tag{3.10}$$

For such an analysis, the governing equation (3.8) is also rewritten as:

$$\begin{aligned} &(a) \quad \nabla^2 \Phi_{n_C} = 0 && 0 \leq y \leq c \\ &(b) \quad \nabla^2 \Phi_{n_L} = 0 && d \leq y \leq d + \Delta \end{aligned} \tag{3.11}$$

Substituting the assumed form for the solution, equation (3.10) into the governing equation and solving determines the potential distribution in terms of four (4) unknown constants. These constants must be determined for each harmonic.

$$\begin{aligned} &(a) \quad \hat{\Phi}_{n_C}(y) = A_{n_C} \cosh k_n y + B_{n_C} \sinh k_n y \\ &(b) \quad \hat{\Phi}_{n_L}(y) = A_{n_L} \cosh k_n y + B_{n_L} \sinh k_n y \end{aligned} \tag{3.12}$$

Boundary Conditions:

As with continuous loading, specification of the potential distribution along the interface and on the outside boundary of the load region provides three (3) of the required four boundary conditions. These can be expressed for each harmonic using Equations (3.7) and (3.12).

$$\begin{aligned} &(a) \quad \hat{\Phi}_{n_C}(y=d) = \hat{v}_n \\ &(b) \quad \hat{\Phi}_{n_L}(y=d) = \hat{v}_n \\ &(c) \quad \hat{\Phi}_{n_L}(y = d + \Delta) = 0 \end{aligned} \tag{3.13}$$

The fourth boundary condition is provided by the charge distribution, again as done in the continuous load case. However, only the fundamental harmonic is involved in matching the channel distribution to the exciting charge wave.

$$\text{(d)} \quad \left.\frac{d\hat{\Phi}_n(y)}{dy}\right)_{y=0} = \frac{-Q_1}{2\varepsilon_o}\,\delta_{-1n}$$

where:

$$\delta_{-1n} = \begin{cases} 1 & n = -1 \\ 0 & n \neq -1 \end{cases}$$

Solutions:

Application of the boundary conditions expressed in Equation (3.13) to the governing equation distributions of equation (3.12) completely specifies the potential distribution in the load and channel regions in terms of the phase complex amplitudes.

$$\hat{\Phi}_{n_C} = \left[\frac{\hat{v}_n}{\cosh k_n d} + \frac{\hat{Q}\,\delta_{-1n}}{2\varepsilon_o k_n}\right] \cosh k_n y - \frac{\hat{Q}\delta_{-1n}}{2\varepsilon_o k_n} \sinh k_n y \qquad (3.14)$$

$$\hat{\Phi}_{n_L} = \hat{v}_n \left[\cosh k_n(y-d) - \coth k_n\Delta \sinh k_n(y-d)\right] \qquad (3.15)$$

where:

$$\hat{v}_n = \sum_{r=1}^{s} \frac{V_r e^{-jk_n rc}}{scbk_n^2}\left[4\, e^{jk_n a/2} \sin\frac{k_n c}{2} \sin\frac{k_n b}{2}\right] e^{jk_n x} \qquad (3.16)$$

as developed in the Fourier analysis section.

Equivalent Circuit:

The analysis involved to obtain an equivalent circuit for the discretely loaded generator is analogous to that followed in Chapter II for the continuum

loaded generator. To characterize the channel and load regions, solve for the net current density normal to the interface as a function of the potential distribution along the electrodes. Then to include the effect of the lumped loading, as shown in Fig. 3.1, consider the ℓth electrode and apply conservation of current.

$$\hat{I}_\ell = \hat{V}_\ell \hat{Y}_\ell = \int_{(\ell-1)c+b}^{\ell c} \left[\sum_{n=-\infty}^{\infty} \hat{J}_n e^{jk_n x} \right] dx \tag{3.17}$$

In the expression the current density is also represented as an infinite series of harmonically related traveling waves. The complex amplitude for each harmonic is determined by the lumped circuit characterization of the load and channel regions.

$$\hat{J}_n = \hat{J}_s - j\omega[C_n + C_n]\hat{v}_n \tag{3.18}$$

The source term is the same form as found in the continuous case.

$$\hat{J}_s = \frac{j\omega\hat{Q}\delta_{-1n}}{2 \cosh k_n d} \text{ amps/m}^2 \tag{3.19}$$

The lumped capacitance characterizing the channel region is:

$$C_{nc} = \varepsilon_o k_n \tanh k_n d \quad \text{farad/m}^2 \tag{3.20}$$

and that characterizing the load region:

$$C_{nL} = \varepsilon_o k_n \coth k_n \Delta \quad \text{farad/m}^2 \tag{3.21}$$

Interchanging the order of summation and integration in Equation (3.17) and carrying out the integration yields:

$$\frac{\hat{V}_\ell \hat{Y}_\ell}{g} = \frac{j\omega\hat{Q}\sin k_1 a/2}{k_1 \cosh k_1 d} e^{-jk_1(\ell c - a/2)} - \omega \sum_{n=-\infty}^{\infty} \frac{\hat{v}_n e^{jk_n \ell c}[C_{nc} + C_{nL}][1 - e^{-jk_n a}]}{k_n} \tag{3.22}$$

Equation (3.22) is the most general form of solution for the voltage on the ℓth electrode as a function of its load admittance, and the voltages and load admittances of all other s - 1 electrodes. It is convenient to consider Equation (3.22) as a vector equation of the form.

$$\begin{bmatrix} a_{11} & a_{12} & --- & a_{1s} \\ a_{21} & & & \\ \vdots & & & \\ a_{s1} & & & a_{ss} \end{bmatrix} \begin{bmatrix} \hat{V}_1 \\ \hat{V}_2 \\ \vdots \\ \hat{V}_s \end{bmatrix} = \begin{bmatrix} \hat{D}_1 \\ \hat{D}_2 \\ \vdots \\ \hat{D}_s \end{bmatrix} \tag{3.23}$$

or in vector notation:

$$\hat{\underline{A}}\ \hat{\underline{V}} = \hat{\underline{D}} \tag{3.24}$$

where the elements of $\hat{\underline{A}}$ are of the form:

$$a_{\ell r} = \left\{ \frac{\hat{Y}_r}{g} \delta_{\ell r} + j\omega\varepsilon_o \sum_{n=-\infty}^{\infty} \frac{8\hat{V}_r}{scbk_n^2}[\tanh k_n d + \coth k_n \Delta] e^{jk_n(\ell - r)c} \left[\sin\frac{k_n a}{2} \sin\frac{k_n b}{2} \sin\frac{k_n c}{2}\right]\right\} \tag{3.25}$$

and of $\hat{\underline{D}}$

$$\hat{D}_\ell = \frac{j\omega Q_1 \sin k_1 a/2}{k_1 \cosh k_1 d} e^{-jk_1(\ell c - a/2)} \tag{3.26}$$

Since the matrix $\hat{\underline{A}}$ is square and therefore in general has an inverse, it is now possible to solve for each of the s electrode voltages and the problem is completely specified and solved.

$$\hat{\underline{V}} = \hat{\underline{A}}^{-1} \hat{\underline{D}} \tag{3.27}$$

This general case would be extremely difficult to solve and is of limited interest. Of prime interest is the case of a uniform loading, all the electrode load admittances identical. In this case the magnitudes of all the V_r's will be identical and they will be shifted in space from each other by some phase angle. This can be shown to be, in fact, the case, by assuming electrode voltages of this form, substituting them into Eq. (3.23) and noting that it then reduces to s identical equations.

Assume:

$$\hat{Y}_\ell = \hat{Y}_o \tag{3.28}$$

and

$$\hat{V}_\ell = \hat{V}_o \, e^{-jk_1(\ell c - a/2)} \tag{3.29}$$

Substituting this into Eq. (3.23) and noting that the doubly infinite sum on n is simply the sum of a complex number and its conjugate, the one remaining equation for the voltage amplitudes is the following:

$$\hat{V}_o = \frac{\dfrac{j\omega\hat{Q} \sin k_1 a/2}{k_1 \cosh k_1 d}}{\dfrac{\hat{Y}_o}{g} + j\omega\varepsilon_o \displaystyle\sum_{r=0}^{s-1} \frac{16e^{-jk_1 rc}}{scb} \sum_{n=0} \frac{[\tanh k_n d + \coth k_n \Delta]}{k_n^2} \cos k_n rc \sin k_n a/2 \sin k_n b/2 \sin k_n c/2} \tag{3.30}$$

This represents the solution that the foregoing analysis had as its objective. It is interesting to note that, in taking the limit as $b \to 0$ and $s \to \infty$, this solution collapses to one identical in form to the one expressed by equations

(2.9) and (2.10).

Equation (3.30) can be represented as an equivalent circuit which characterizes the discretely loaded generator in lumped elements on a per meter of channel depth basis.

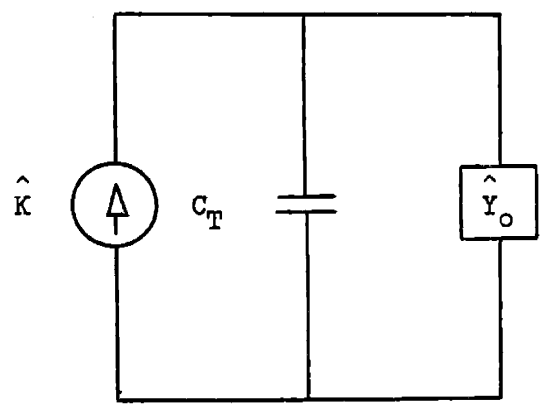

Figure 3.4

where:

$$C_T = \varepsilon_o g \sum_{r=0}^{s-1} \frac{16e^{-jk_1 rc}}{scb} \sum_{n=0}^{\infty} \frac{[\tanh k_n d + \coth k_n \Delta]}{k_n^2} \cos k_n rc \sin \frac{k_n a}{2} \sin \frac{k_n b}{2} \sin \frac{k_n c}{2} \quad \text{farads}$$

and the source is defined:

$$\hat{K} = \frac{j\omega \hat{Q} g \sin k_1 a/2}{k_1 \cosh k_1 d} \quad \text{amps} \qquad (3.32)$$

Power Output:

Using the equivalent circuit of Fig. 3.4, the output power for the discretely loaded generator is readily calculated. Since only the upper half of the generator was analyzed, this power figure must be multiplied by two in order to give the total power output. Consider pure resistive loading $\hat{Y}_o = G_o$, then:

$$< P > = \frac{G_o |\hat{K}|^2}{G_o^2 + \omega^2 C_T^{\,2}} \text{ watts/electrode} \tag{3.33}$$

Power Optimization:

As with the continuous load case, there is a matched loading which produces optimum power output.

$$G_{OPT} = \omega C_T \text{ mhos} \tag{3.34}$$

For this load, the optimum power becomes:

$$< P >_{OPT} = \frac{|\hat{K}|^2}{2\omega C_T} \text{ watts/electrode} \tag{3.35}$$

where K and C_T have been defined in Equations (3.32) and (3.31).

Comparison of Discrete and Continuously Loaded Generators:

Having developed the theory for both the continuously loaded and the discretely loaded generators, it is now possible to make some comparisons between the two arrangements. In particular, it is of interest to examine the difference in characteristic internal capacitance and optimum power outputs. In order to make such comparisons, it is helpful to rearrange Equation (3.30) into a form that is normalized to electrode area.

$$\hat{V}_o = \frac{\dfrac{j\omega\hat{Q}}{2 \cosh k_1 d} \left[\dfrac{\sin k_1 a/2}{k_1 a/2}\right]}{\dfrac{Y_o}{ag} + j\omega\varepsilon_o k_1 \displaystyle\sum_{n=0}^{\infty} \sum_{r=0}^{s-1} 2n \left[e^{-jk_1 rd} \cos k_n rc\right] \left[\tanh k_n d + \coth k_n \Delta\right] f(n)} \tag{3.36}$$

where $$f(n) = \frac{\sin k_n a/2}{k_n a/2} \; \frac{\sin k_n b/2}{k_n b/2} \; \frac{\sin k_n c/2}{k_n c/2}$$

The sum over r in the denominator of this equation may be rewritten and the result used in defining a characteristic internal capacitance for the discretely

loaded generator.

$$C_D = \varepsilon_o k_1 \sum_{n=0}^{\infty} \sum_{r=0}^{s-1} 2n[\cos k_n rc \cos k\ rc][\tanh k_n d + \coth k_n \Delta]\ f(n) \text{ farads/m} \tag{3.37}$$

Recalling from Chapter II that the characteristic internal capacitance for the continuously loaded generator is given by:

$$C_C = \varepsilon_0 k_1 [\tanh k_1 d + \coth k_1 \Delta] \text{ farads/m}^2 \tag{3.38}$$

a ratio which compares these capacitances is defined:

$$\text{CAPR} = \frac{C_C}{C_D} \tag{3.39}$$

Before making a comparison of optimum power outputs, note that the total channel area over which power is delivered to the loading is not the same in the two types of generator, and the difference must be taken into consideration. The amount of this difference is reflected in the ratio of discrete electrode width (a) to the fundamental wavelength divided by the number of phases (c).

$$\alpha = a/c \tag{3.40}$$

Taking into account the relative area factor, a ratio comparing the optimum power outpute may be defined using the optimum power output expressions for the discretely and continuously loaded generator as given by Equations (3.33) and (2.16) respectively.

$$\text{POWR} = \frac{\langle P \rangle_{\text{OPT DISCRETE}}}{\langle P \rangle_{\text{OPT CONTINUOUS}}} = \left[\frac{\sin k_1 a/2}{k_1 a/2}\right]^2 \left[\frac{C_C}{C_D}\right] \tag{3.41}$$

Due to the double sums involved in the above ratios, the computer was used to make sample calculations for curve plotting, and the programs designed and employed for this purpose are contained in Appendix C.

Curves 3.1 and 3.2 demonstrate how the ratios expressed in Eq. (3.39) and Eq. (3.41) vary according to the number of phases used per wavelength and the degree to which the discrete electrodes occupy the channel interfacial area. It should be emphasized that these curves are only as good as the model from which they were obtained. For this reason, they should not be expected to give valid results at the extremes of the ranges.

The range of α studied is felt to correspond to that range over which the discrete generator model is valid. From curve 3.1, note that CAPR is a maximum overall s for $\alpha = .5$, and decreases symmetrically for α greater or less than this value.

Curve 3.2 demonstrates the effects of α and s on output power. It appears from these curves that large α and s would be the most desirable arrangement. The power ratio goes asymptotically to α as s is increased to large values and is always less than α due to the area difference between discrete and continuous loading. However, as α and s are increased, the spacing gets very small and electric field breakdown strength becomes of critical importance.

Using curve 3.2, one is led to make the optimistic judgment that discretely loaded charge-constrained generators compare very favorably with continuously loaded ones on the basis of power output. An energy conversion efficiency which quantifies the degree to which the maximum amount of power available is removed from a discretely loaded generator as a function of α and s is displayed on curve 3.3. The information used to plot this

curve is contained in curve 3.2 and is not a reflection of mechanical to electrical conversion efficiency. All generators considered are assumed to be 100 per cent efficient in this regard, as no losses have been included in the model.

Experiments on an actual generator are now in order so that the theory on which the preceding calculations are based may be verified.

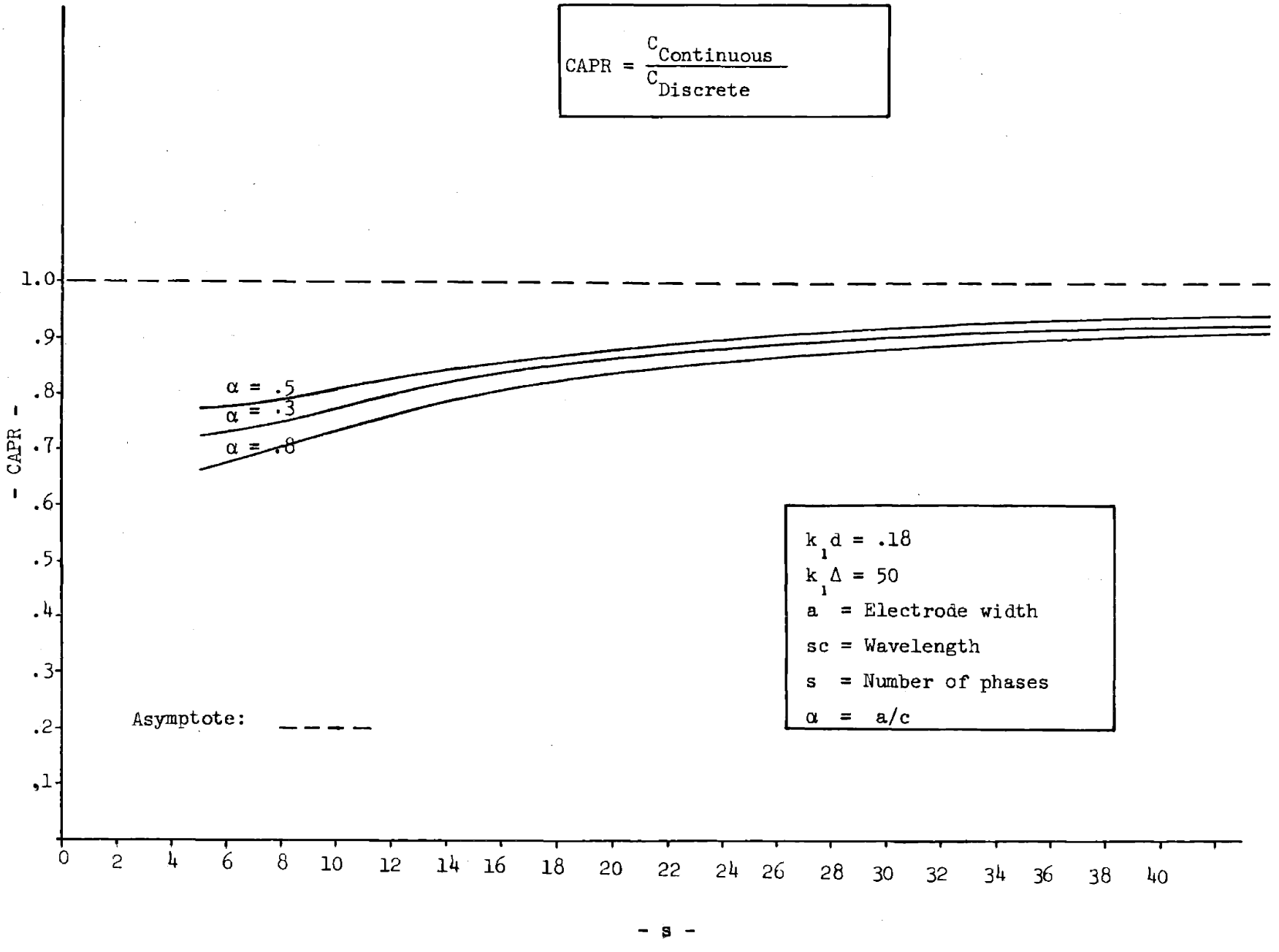
CAPR = C Continuous / C Discrete
1.0
.9
.8
.7
.6
.5
.4
.3
.2
.1
- CAPR -
α = .5
α = .3
α = .8
Asymptote:
k1d = .18
k1Δ = 50
a = Electrode width
sc = Wavelength
s = Number of phases
α = a/c
0 2 4 6 8 10 12 14 16 18 20 22 24 26 28 30 32 34 36 38 40
- s -

Curve 3.1

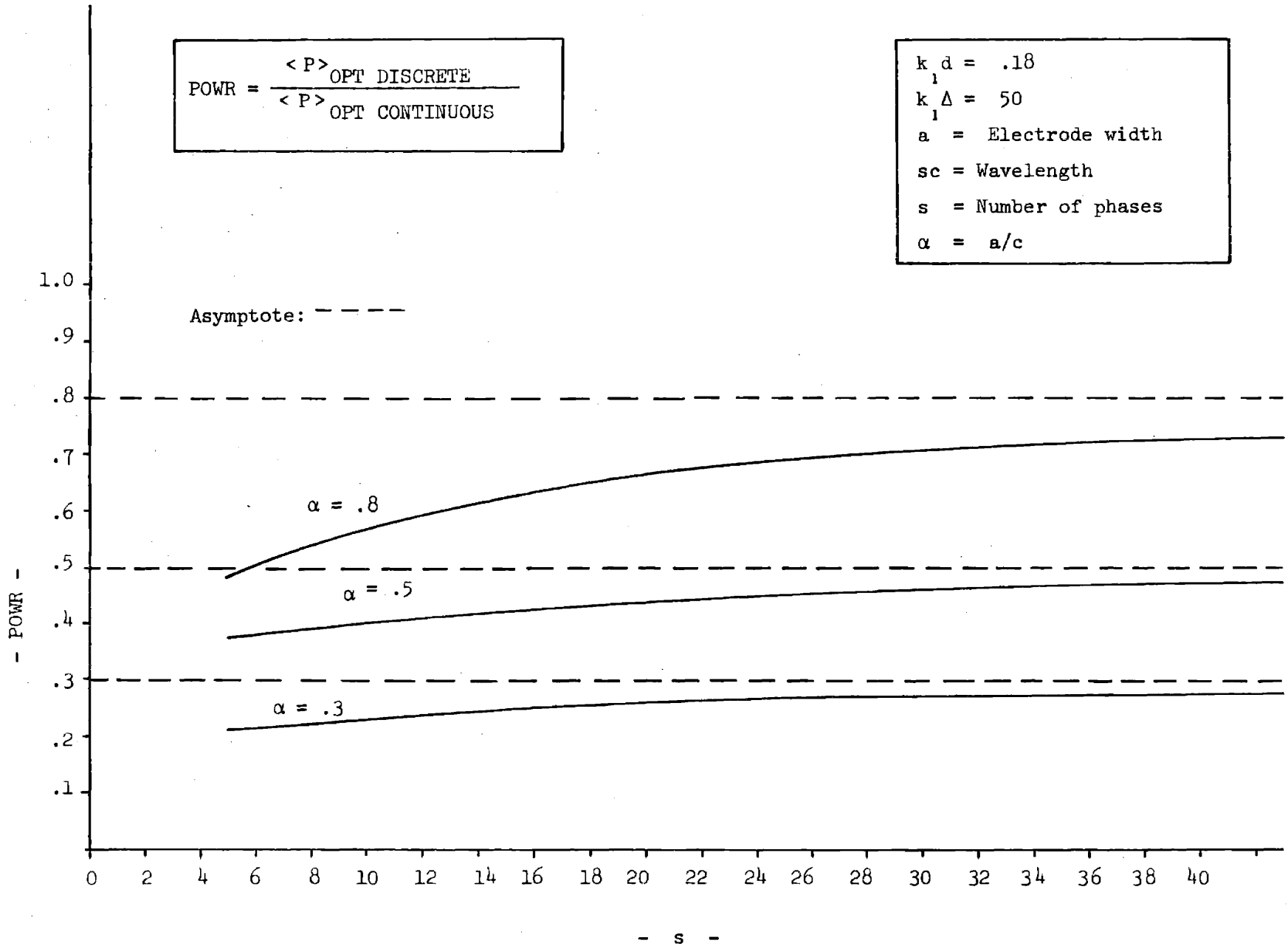
POWR = <P>OPT DISCRETE / <P>OPT CONTINUOUS
k1d = .18
k1Δ = 50
a = Electrode width
sc = Wavelength
s = Number of phases
α = a/c
Asymptote:
α = .8
α = .5
α = .3
- POWR -
1.0
.9
.8
.7
.6
.5
.4
.3
.2
.1
0 2 4 6 8 10 12 14 16 18 20 22 24 26 28 30 32 34 36 38 40
- s -

Curve 3.2

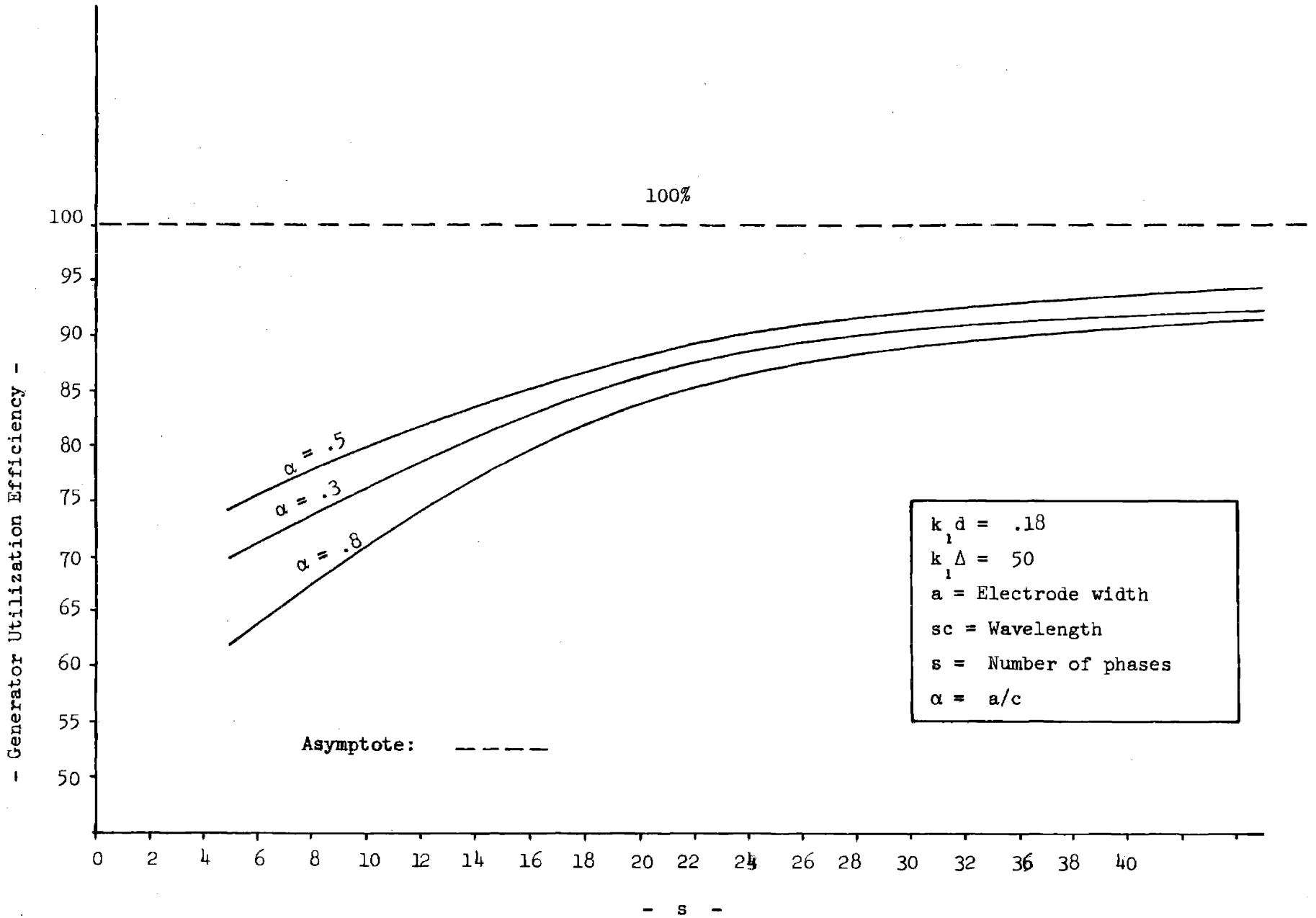
100%
100
95
90
85
80
75
70
65
60
55
50
- Generator Utilization Efficiency -
α = .5
α = .3
α = .8
Asymptote:
k1d = .18
k1Δ = 50
a = Electrode width
sc = Wavelength
s = Number of phases
α = a/c
0 2 4 6 8 10 12 14 16 18 20 22 24 26 28 30 32 36 38 40
- s -

Curve 3.3

CHAPTER IV

EXPERIMENTAL COMPARISON WITH THEORETICAL PREDICTIONS

Introduction:

In Chapter III, a general theory was developed for determining the loading characteristics of the charge-constrained synchronous generator. Modifications to this theory, to account for the geometry of the experimental generator, have been developed and are presented in Appendix A. It is now possible to present a theory which applies strictly to the laboratory generator and to make predictions concerning its output characteristics.

From Equation (3.30), the output voltage for any electrode in the uniform loading situation is:

$$\hat{V}_o = \frac{\hat{D}}{\frac{\hat{Y}_o}{g} + j\omega \sum_{r=0}^{s-1} \frac{16\, e^{jk_1 rc}}{scb} \sum_{n=0}^{\infty} \frac{[C_{n_C} + C_{n_L}]}{k_n^3} f(n)} \tag{4.1}$$

where:

$$f(n) = \cos k_n rc \sin k_n a/2 \quad \sin k_n b/2 \quad \sin k_n c/2 \tag{4.2}$$

In Appendix A, the modifications for $\hat{D}$, C_{n_C} and C_{n_L} are developed, taking into account the character of the actual channel. The result for the source term, using (A.11), was:

$$\hat{D} = \frac{j\omega\hat{Q}\, 2 \sin k_1 a/2}{k_1 \cosh k\, d[1 + \varepsilon_r f_1 \tanh k_1 d]} \tag{4.3}$$

The modified capacitance for the channel is:

$$C'_{n_C} = \frac{\varepsilon_o k_n [\varepsilon_r f_1 + \tanh k_n d]}{[1 + \varepsilon_r f_1 \tanh k_n d]} \tag{A.10}$$

and for the load region, the capacitance becomes:

$$C'_{n_L} = \frac{\varepsilon_p k_n [\coth k_n\delta + \varepsilon_r]}{[1 + \varepsilon_r \coth k_n\delta]} \tag{A.5}$$

where the following definitions have been used:

$$f_1 = \frac{1 + \varepsilon_r \tanh k_n(h-\delta)\tanh k_n\delta}{\varepsilon_r \tanh k_n(h-\delta) + \tanh k_n\delta} \tag{A.12}$$

and

$$\varepsilon_r = \varepsilon_p/\varepsilon_o \tag{A.6}$$

For the laboratory generator as described in appendix B, the following geometrical factors apply:

a) $\varepsilon_r = 4$

b) $\overline{k}_n\delta = .213\ n$

c) $\overline{k}_n(h-\delta) = 3.87\ n$

d) $\overline{k}_n d = .177\ n$

e) $\overline{k}_n = 33.8\ n$

f) Area of electrode = $11.5 \times 10^{-4}\ m^2$

Short Circuit Current Measurement and Charge Prediction:

For the purposes of this chapter, consider the following circuit model for each generator electrode and its load.

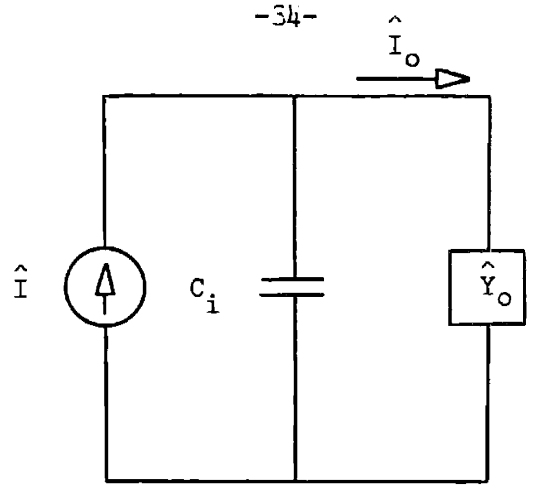

Where the circuit quantities are defined from Equation (4.1). and Appendix A.

$$\hat{I} = g\,\hat{D}' \tag{4.5}$$

and the internal capacitance.

$$C_i = g \sum_{r=0}^{s-1} \frac{16\, e^{jk_1 rc}}{scb} \sum_{n=0}^{\infty} \frac{[C'_{n_C} + C'_{n_L}]}{k_n^3} f(n) \tag{4.6}$$

Now, using Equation (4.5) it is possible to make measurements of the short circuit current and predict the magnitude of the charge density on the disk. This prediction can then be compared with the actual disk charge density as measured with the electrometer circuit described in Appendix B.

From Eq. (4.1) (4.5) and (4.6), we have:

$$\hat{I}_o = \frac{g\,\hat{D}'\,\hat{Y}_o}{\hat{Y}_o + j\omega C_i} \tag{4.7}$$

and for the case where

$$\hat{Y}_o/\omega C_i >> 1 \tag{4.8}$$

the output current will, to a very good approximation, be the short circuit current.

The inequality of Eq. (4.8) was obtained

on the experimental generator by loading with a pure resistance that gave:

$$Y_o = 2 \times 10^{-7} \text{ ohms} \tag{4.9}$$

It will become clear later that this loading does indeed satisfy the condition imposed by Eq. (4.8).

To determine the relationship between the short circuit current and the surface charge density, recall:

$$|\hat{I}| = \frac{2g\omega \sin k_1 a/2 \; |\hat{Q}|}{k_1 \cosh k_1 d[1 + \varepsilon_r f \tanh k_1 d]} \tag{4.10}$$

Since the electrode current is given by the integral of the current density over the area of the electrode, and since the dimensions of the electrodes vary due to the cylindrical arrangement, it is appropriate to let

$$g = \frac{\text{Area of Electrode}}{a} \tag{4.11}$$

where a is the electrode width over which the integration (3.17) was carried out.

Using the numerical values presented in Eq. (4.4), a relationship for predicting the disk surface charge density from the source (i.e., short circuit) current is obtained. Evaluation yields:

$$|\hat{Q}| = 3.41|\hat{I}| \quad \text{coul/m}^2 \tag{4.12}$$

The following short table compares the magnitude of the surface charge density as predicted from the short-circuit current and that measured with the electrometer to demonstrate the validity of equa-

tion (4.12). Several of these comparisons were carried out over a period of time, and the results were consistent and reproduceable.

$\lvert\hat{Q}\rvert$ predicted (coul/m^2)	$\lvert\hat{Q}\rvert$ measured (coul/m^2)
24.0×10^{-6}	24.8×10^{-6}
15.0×10^{-6}	15.8×10^{-6}
23.9×10^{-6}	24.8×10^{-6}

Table 4.1

A representative distribution of surface charge density as a function of angle around the source disk, as obtained by electrometer measurements, is given on Graph (4.1)

Evaluation of Internal Capacitance Predicted by Theory:

The theory predicts an internal capitance for the generator that is expressed by Equation (4.6). Since the terms of the infinite series go as $1/n^2$ and the series contains terms of alternating signs, it is expected to converge very rapidly, making the evaluation of the internal capacitance through truncation efficient. In addition, further examination of the series over the r variable exposes the fortunate fact that terms in the double series have value only for particular values of n. To show this, interchange the order of summation in Equation (4.6) to get:

$$C_i = g \sum_{n=0}^{\infty} \frac{16[C'_{n_C} + C'_{n_L}]}{scb\ k_n^3} \sin\frac{k_n a}{2} \sin\frac{k_n b}{2} \sin\frac{k_n c}{2} \left[f_2(n) \right] \tag{4.13}$$

where
$$f_2(n) = \sum_{r=0}^{s-1} \frac{e^{j2\pi\frac{(n+1)r}{s}} + e^{-j2\pi\frac{(n-1)r}{s}}}{2} \tag{4.14}$$

In Eq. (4.14) the exponential form of $\cos k_n rc$ and the definition of Eq. (3.4) have been used.

Examination of Eq. (4.14) reveals:

$$f(n) = \begin{cases} 3 & n=1;\ \frac{n+1}{s} = m;\ \frac{n-1}{s} = m \qquad m = 1,2,3 \ldots\ldots \\ 0 & \text{otherwise } (\Sigma \text{ of s roots of 1}) \end{cases} \tag{4.15}$$

This of course greatly facilitates the evaluation of the internal capacitance predicted by the theory. For the case s = 6:

$$C_i = \frac{8g}{cb} \sum_{n=0}^{\infty} \frac{[C'_{n_C} + C'_{n_L}]}{k_n^3} \sin\frac{k_n a}{2} \sin\frac{k_n b}{2} \sin\frac{k_n c}{2} \tag{4.16}$$

$$n = 1,5,7,11,13,17,19 \text{ ----}$$

Using the physical characteristics of the generator as presented in Appendix B and truncating the infinite series, one obtains for the internal capacitance associated with each electrode, as predicted by the theory:

$$C_i = 4.7 \times 10^{-12} \text{ farads}$$

Sources of Capacitance Not Accounted for in Theory:

The theory as modified in Appendix A does not fully account for all the capacitance that characterizes the generator. The most significant source of capacitance unaccounted for in the theory has to do with the finite dimension of the electrodes in the vertical coordinate and the

screws and nuts used to secure them to the load disk. Consider Fig. 4.1.

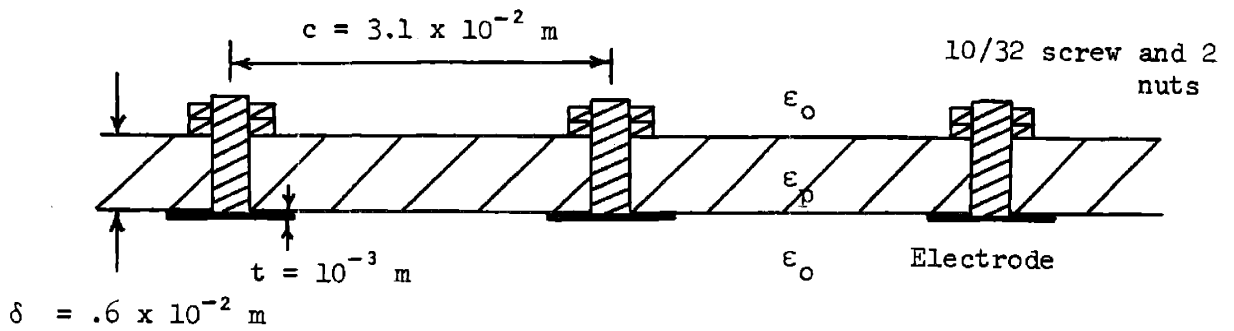

Figure 4.1

It would be extremely difficult to perform an exact calculation to determine the amount of this capacitance; however, approximate evaluations may be made readily. Consider the circuit demonstrating the effects about any electrode as in Fig. 4.2.

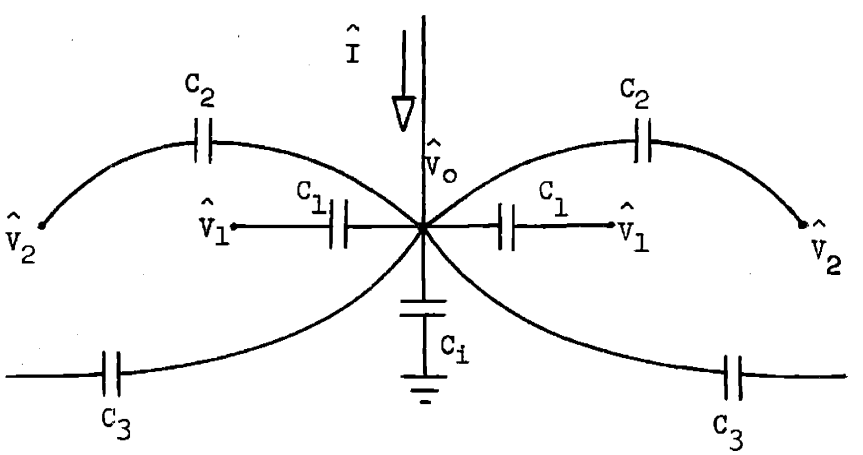

Figure 4.2

Recalling the phase shift between electrode voltages, the added capacitance due to the structure is given by (4.18) considering the associated resistance ($\sim 10^{10}$ ohms) as an open circuit.

$$C_s = 2[C_1(1 - \cos\frac{\pi}{3}) + C_2(1 - \cos\frac{2\pi}{3}) + ---] \qquad (4.18)$$

Using the impedance bridge, it was possible to get an experimental measurement of the capacitance involved in Equation (4.18)

$$C_1 = 1.5 \text{ pf}$$
$$C_2 = .75 \text{ pf}$$
$$C_3 = .25 \text{ pf}$$
$$C_4 \cong 0$$

Using these results:

$$C_s \cong 4.8 \times 10^{-12} \text{ farads} \tag{4.19}$$

Unfortunately this capacitance is approximately equal in magnitude to that predicted by the theory as inherent to the generator. However, any structure that might be devised to hold the electrodes would have some capacitance associated with it. With both the internal and structural capacitances so small, the result of any attempt to further reduce them would be difficult to detect. The structure capacitance was included in the equivalent generator circuit used to predict output. This total capacitance was considered as the characteristic capacitance of each electrode.

$$\begin{aligned} C_T &= C_i + C_s \\ &= 9.5 \times 10^{-12} \text{ farads} \end{aligned} \tag{4.20}$$

Prediction of Matching Load

The experimental generator contains five wavelengths of electrodes with six (6) electrodes per wavelength, as is described in Appendix B. To avoid the problems involved in loading each electrode as a separate source, the experiments were conducted with electrode outputs of the same phase connected in parallel. This required the attachment of only six

loads to obtain characterizing output data. The modifications to the generator equivalent circuit are obvious:

$$\begin{aligned} &(a) \quad \hat{I} \rightarrow 5\,\hat{I} \\ &(b) \quad C_T \rightarrow 5\,C_T \\ &(c) \quad \hat{Y}_o \rightarrow 5\,\hat{Y}_o \end{aligned} \tag{4.21}$$

Using the generator so configured, that is, like phase assembled in parallel, it was possible to predict the loading for maximum power output using the results of Chapter III and Equation (4.20).

$$(a) \quad Y_{L_{OPT}} = 5\,\omega\,C_T \text{ mhos} \tag{4.22}$$

and for $\omega = 377$ rad/sec

$$(b) \quad Y_{L_{OPT}} = 17.9 \times 10^{-9} \text{ mhos}$$

and

$$(c) \quad R_{L_{OPT}} = 56 \times 10^{6} \text{ ohms}$$

This represents the loading that is predicted by the theory for the generator to produce maximum power with five electrodes of the same phase wired in parallel. On a per-electrode basis, if each electrode was loaded individually, the required loading is as predicted in Equation (4.21):

$$R_{L_{OPT}} = 280 \times 10^{6} \text{ ohms} \tag{4.23}$$

The effect of parallel operation in determining the matched load condition increases the flexibility in application of such generators.

Experimental Determination of a Matched Load:

To obtain the output data from the experimental generator, for the purpose of identifying the actual internal capacitance, it was wired in parallel, as described in the previous section.

The scheme employed to determine the matching resistive load (and thus the total characteristic capacitance) was to examine a log-log plot of output current magnitude versus resistance loading magnitude. Consider the magnitude of the output current as a function of the source current, total capacitance and loading:

$$|\hat{I}_o| = \frac{|\hat{I}|\left(\frac{1}{\omega c}\right)}{\left[R_L^2 + \frac{1}{\omega^2 c^2}\right]^{1/2}} \qquad (4.24)$$

where $k = \frac{1}{\omega c}$

taking the $\log_{10}$ of both sides.

$$\log_{10} |\hat{I}_o| = \text{constant} - \frac{1}{2} \log_{10} [R_L^2 + K^2] \qquad (4.25)$$

From this, two limiting cases become apparent as R_L is varied over a wide range. First:

$$R_L^2 >> \frac{1}{\omega^2 c^2} \; ; \; \frac{\log_{10}|\hat{I}_o|}{\log_{10} R_L} = -1 \qquad (4.26)$$

and

$$R_L^2 >> \frac{1}{\omega^2 c^2} ; \; \frac{\log_{10}|\hat{I}_o|}{\log_{10} R_L} = 0 \qquad (4.27)$$

By plotting $\log_{10} |\hat{I}_o|$ as the ordinate and $\log_{10} R_L$ as the abcissa, the value of internal plus structural capacitance can be found graphically. This was done on graph 4.2 As indicated, the characteristic capacitance found was:

$$C_T = 9.65 \times 10^{-12} \text{ farads} \qquad (4.28)$$

To verify this capacitance, several runs were made with the results consistent and reproduceable. A load capacitance was also added in parallel, with the characteristic capacitance and the results were almost exactly as predicted; see graph 4.3.

The power output curve as a function of loading was also calculated and plotted on graph 4.4. Note that the maximum power output occurs at matched loading.

Discussion of Results:

The validity of the theoretical model assumed to characterize the charge-constrained generator has been demonstrated in the previous sections. In particular, the magnitude of the equivalent current source may be accurately predicted by the theory for a known surface charge density.

The experiments have shown the actual internal capacitance to be approximately twice that which would be predicted by the theory alone. However, this predicted capacitance did not include that capacitance associated with the structure of the generator. When this extra capacitance had been estimated and included as part of the characteristic internal capacitance of the generator, then the theoretical prediction accurately matched the actual generator characteristics. However, it is felt that the most accurate method of characterizing a generator in terms of equivalent circuit elements, for application, would be to obtain a plot of equation (4.24). The theory serves the purpose of providing an approximation of the capacitance for design purposes, but due to the structure the actual capacitance would have to be determined after construction. This does not differ from the procedure followed for designing and characterizing magnetic field machines.

$$Q = \frac{\text{Electrometer Reading}}{\text{Area of Probe}} \ \text{coul/m}^2$$

Area of probe = 5.25×10^{-4} m^2

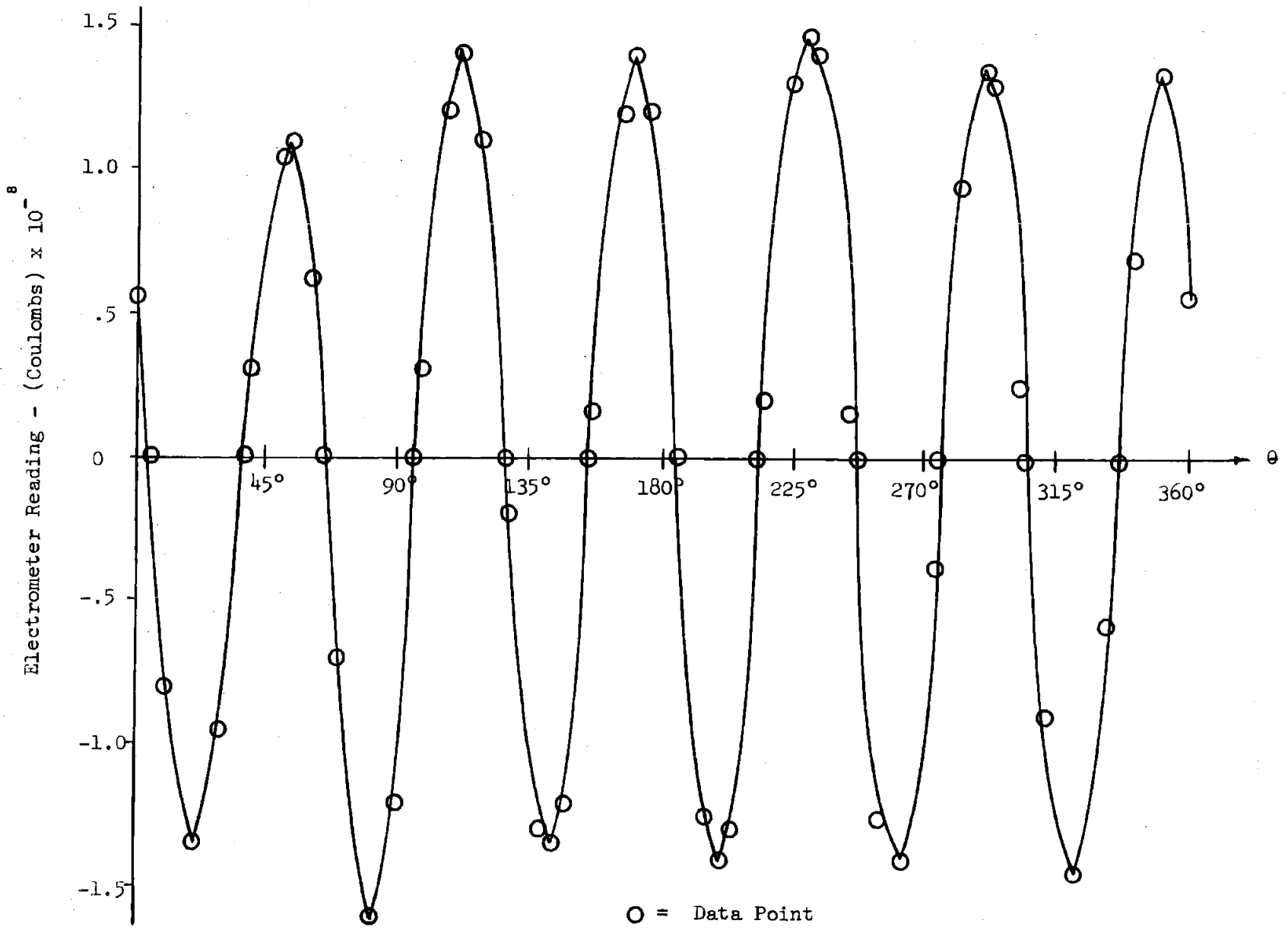

θ = Angular Position on Disk

Curve 4.1: Disk Charge Distribution

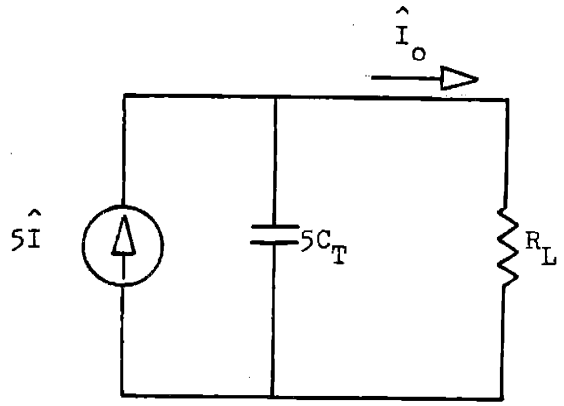

ω = 377 rad/sec

$R_{L_{OPT}}$ = 56×10^6 ohms

$5C_T$ = 47.5 pf

$$\frac{1}{R_{L_{OPT}}} = 5 \quad C_T$$

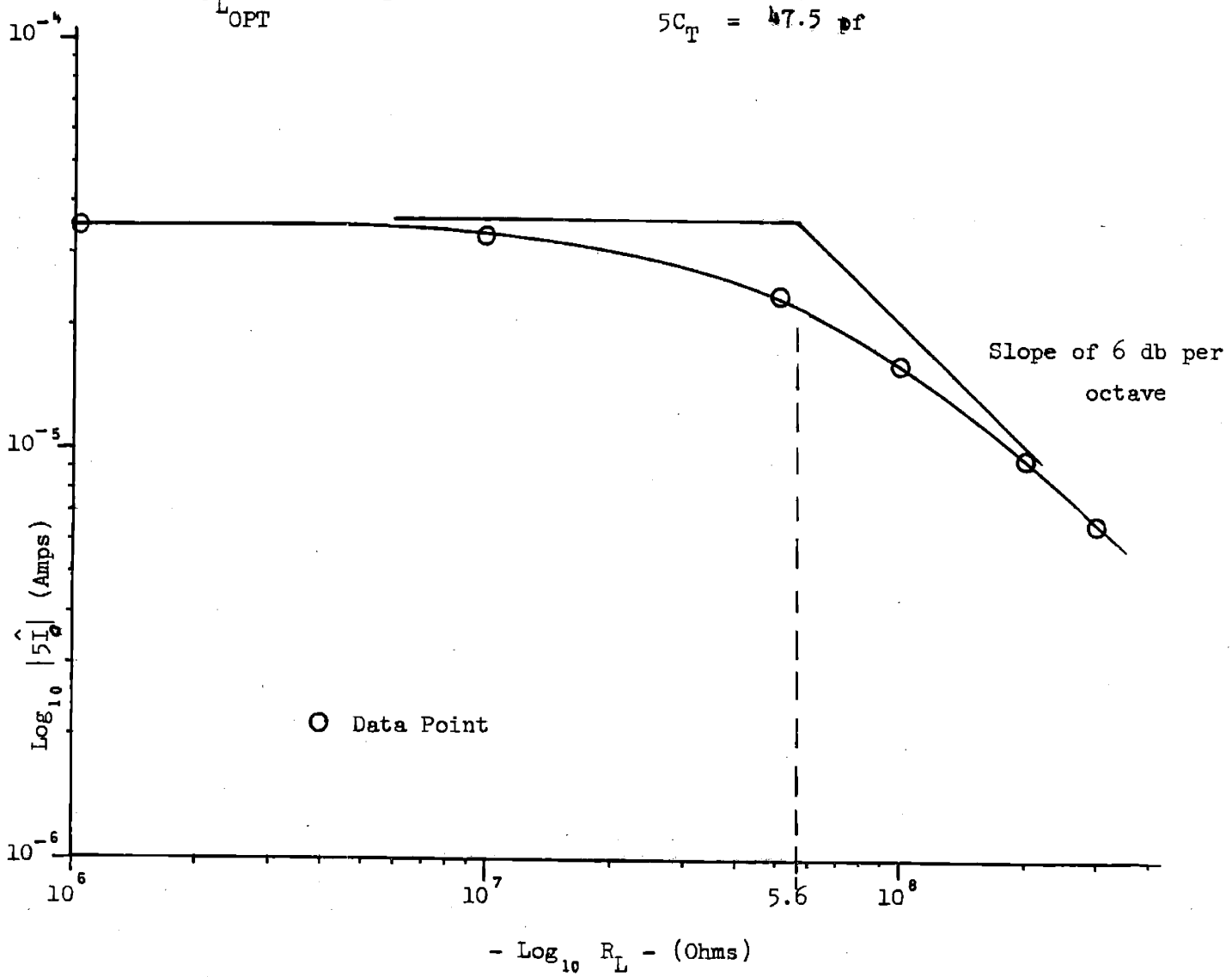

Curve 4.2

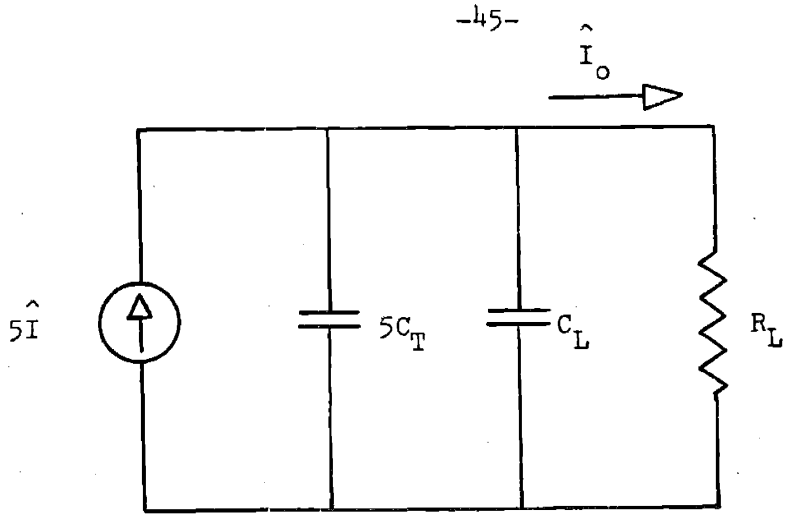

ω = 377 rad/sec

C_L = 50 pf

$R_{L_{OPT}}$ = 27×10^6 ohms

$5C_T$ = 48 pf

$$\frac{1}{R_{L_{OPT}}} = \omega[5C_T + C_L]$$

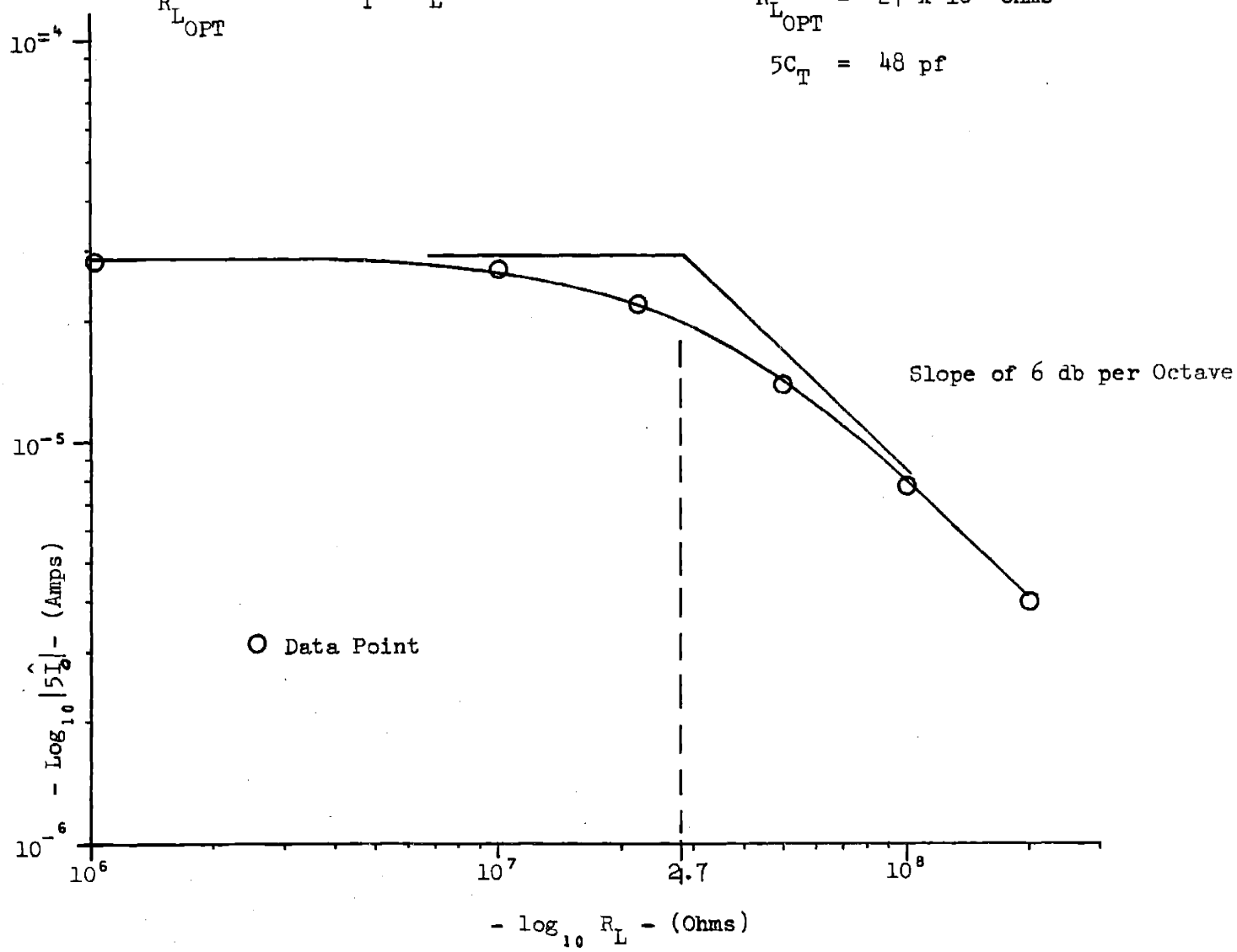

Curve 4.3: Determination of Characteristic Capacitance with Capacitance in the Loading

Power Output per 5 Electrodes Vs Load R_L

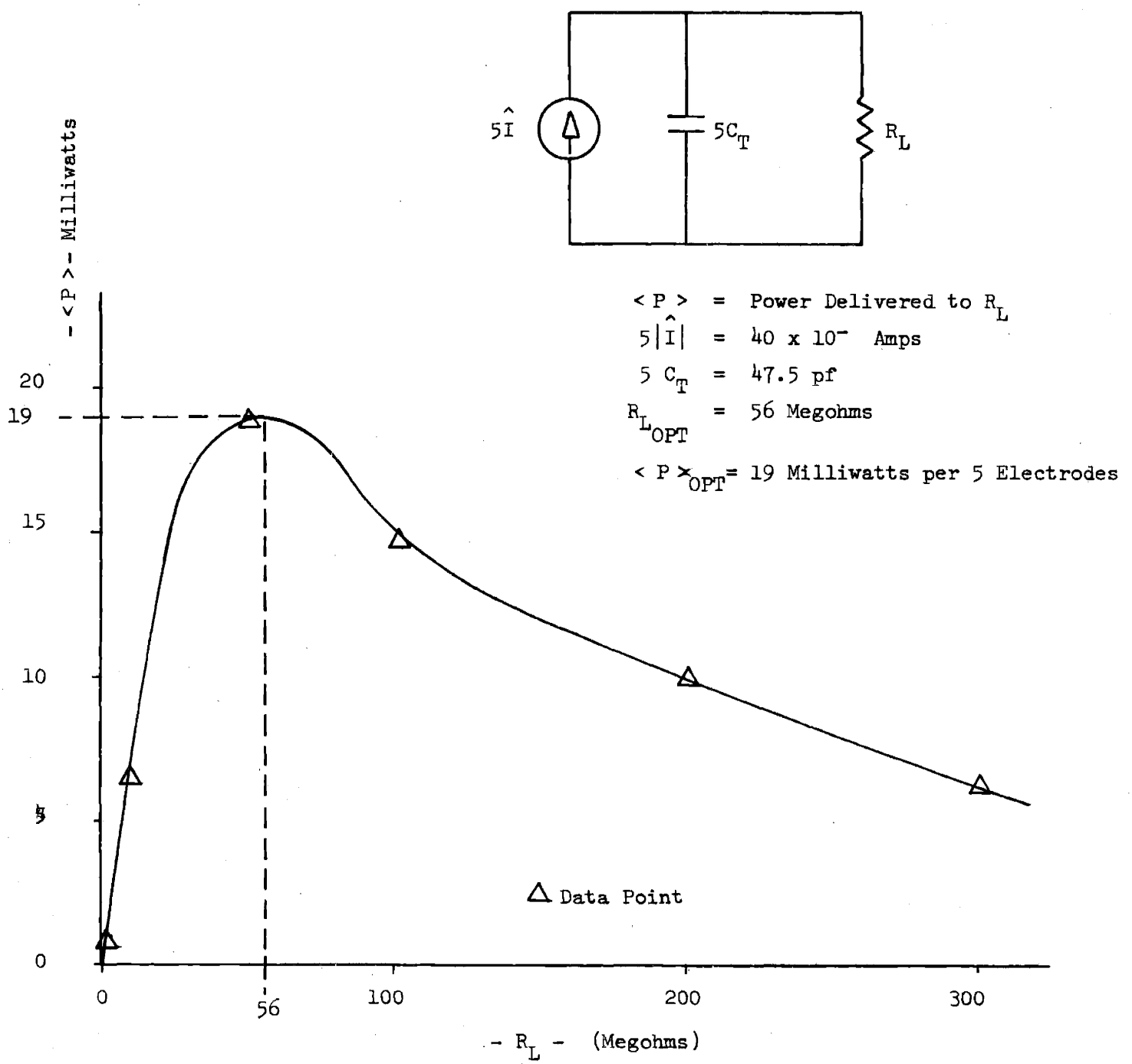

Curve 4.4

CHAPTER V

Conclusion:

The application of charge-constrained synchronous generators in the production of large amounts of electrical power is to a great extent dependent on the feasibility of power removal with a finite number of discrete electrodes. That is, such generators must have output terminals with a finite number of phases through which they can deliver power. Otherwise, they are strictly limited to continuum type loading.

In Chapter III a discretely loaded generator with an arbitrary number of phases was analyzed. By modeling the potential distribution between adjacent electrodes as a linear function, it was possible to obtain a terminal pair representation for each electrode's output. The equivalent circuit for each electrode was shown to be accurately represented by a current source in parallel with a characteristic internal capacitance. It was then demonstrated in Chapter IV that the magnitudes of both of these equivalent lumped elements was accurately predicted by the theoretical model. The need for a means of obtaining an accurate estimation of that part of the internal capacitance due to the physical structure of the load electrodes was demonstrated in the experimental section of this research.

Of prime interest in the use of discretely loaded generators is the amount of power diminution that occurs comparative to the case of continuous loading. It has been shown that this penalty need not be severe if the electrode spacing and number of phases are carefully chosen. With the power output per fundamental wavelength of channel length directly propor-

tional to the electrode area it becomes important to make the inter-electrode spacing as small as field breakdown strength will allow. It is this factor which has the most significant effect in reducing power output when using discrete vice continuous loading.

It has been shown theoretically that a discretely loaded generator can perform efficiently as an energy converter. However, in this regard there are several unanswered questions which may serve as the basis for further investigations in the development of a practical system. The ability of such a generator to run self-excited, from start-up, is of obvious interest. Mechanical energy storage schemes have been proposed[12] to accomplish just this, but is is yet to be demonstrated on an actual device. Questionable is the feasibility of constructing a generator with rotational speeds in excess of 30,000 rpm and providing it with a high vacuum environment so that high electric field intensities may be supported. And lastly is the obvious problem as yet unconsidered, of adapting a six-phase plus generator to provide power for a three-phase world. Needed for this is a very efficient, lightweight phase transformer or system of capacitors which would combine the phases.

APPENDIX

APPENDIX A

Modification to Theory for Experimental Generator

Introduction

For the generator built to provide experimental verification of the theoretical model considered in Chapter III, it was necessary to make some changes to the load and channel arrangements. Practical consideration dictated that the channel be asymmetrically loaded and that plexiglas disks be used to support the electrodes and to carry the exciting charge distribution. These changes do affect the field distribution, and therefore must be reflected in any theory applied to predict output for this particular generator. Conceptually there are no changes; however, the equivalent source and internal capacitance-lumped elements predicted in Chapter III must be modified. A cross-sectional view of the laboratory generator is given in Figure A.1, and demonstrates these changes.

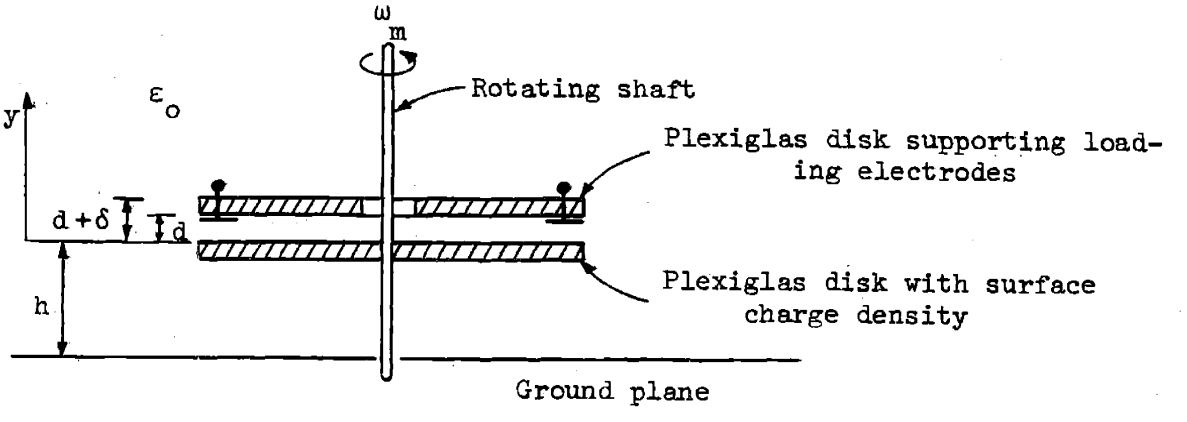

Figure A.1

Appendix A

Since the voltage distribution along the electrodes is assumed known, it is efficient to consider the modifications to the theory in two steps. First, consider the effect of the plexiglas layer above the electrodes on the characteristic capacitance of the load C_{nL}, as defined in Chapter III. Secondly, consider the effect of the plexiglas layer below the electrodes and the asymmetric loading on the source term $\hat{J}_S$, and characteristic channel capacitance C_{nC}, both as defined in Chapter III. These modified equivalent lumped elements should be used in making theoretical predictions for the experimental generator.

Effect of Plexiglas Layer Above Electrodes

The theoretical developments for this and the next section are carried out using techniques identical to those used in Chapter III. Any question concerning procedure should be referred to this chapter, as it is not felt to be necessary to go into the same amount of detail in the expositions of this appendix.

The geometry of the problem being considered is shown in Figure A.2.

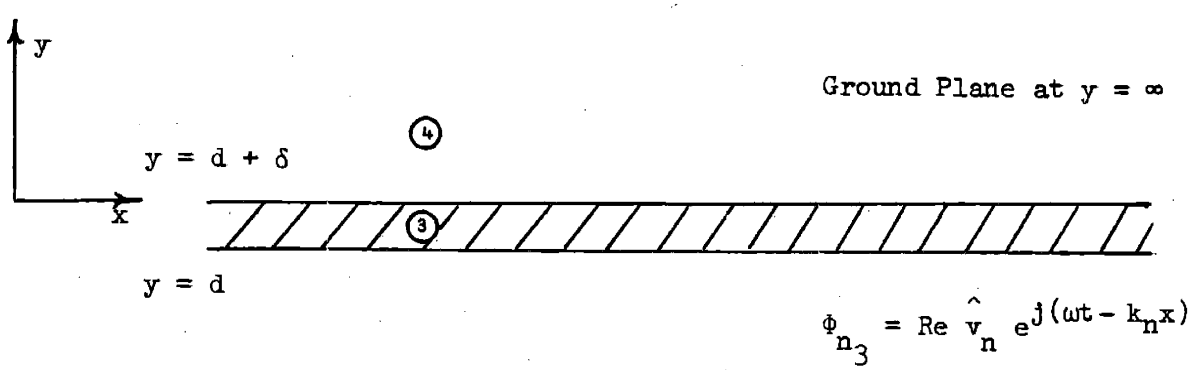

Figure A.2

Appendix A

This is a two-region problem governed by Laplace's equation and therefore the harmonic traveling wave solution will be of the form:

$$\text{(a)} \quad \hat{\Phi}_{n3} = A_{n3} \sinh k_n(y-d) + B_{n3} \cosh k_n(y-d) \qquad d \leq y \leq d+\delta$$

$$\text{(b)} \quad \hat{\Phi}_{n4} = A_{n4}\, e^{-k_n(y-d-\delta)} \qquad \text{(A.1)}$$

where the boundary condition of zero potential at $y = \infty$ has been used and the solution axes have been shifted to make calculation more efficient.

The three remaining boundary conditions which specify this problem are given by

$$\text{(a)} \quad \hat{\Phi}_{n3}(y = d+\delta) = \hat{\Phi}_{n4}(y = d+\delta)$$

$$\text{(b)} \quad \varepsilon_p \nabla_y \hat{\Phi}_{n3}\Big)_{y=d+\delta} = \varepsilon_o \nabla_y \hat{\Phi}_{n4}\Big)_{y=d+\delta} \qquad \text{(A.2)}$$

$$\text{(c)} \quad \hat{\Phi}_{n3}(y=d) = \hat{v}_n$$

Using the boundary conditions (A.2) to evaluate the unknown constants of (A.1) completely determines the fields. Using these results, it is now possible to obtain the modified expression for the load capacitance C_{nL} by considering the displacement current density normal to the channel axis at the electrode interface

$$\hat{J}_n = -j\omega\varepsilon_p \left[\nabla_y \hat{\Phi}_{n3}\right]_{y=d} \qquad \text{(A.3)}$$

and

$$C'_{nL} = -\varepsilon_p \left[\nabla_y \hat{\Phi}_{n3}\right]_{y=d} \qquad \text{(A.4)}$$

Completing these calculations yeilds the modified capacitance.

Appendix A

$$C'_{nL} = \frac{\varepsilon_p k_n [\coth k_n \delta + \varepsilon_r]}{[1 + \varepsilon_r \coth k_n \delta]} \text{ farads/m}^2 \tag{A.5}$$

where $\varepsilon_r = \varepsilon_p / \varepsilon_o$ (A.6)

Effect of Asymmetric Loading and Plexiglas Charge Disk:

Evaluation of the effects of asymmetric loading and the plexiglas charge disk requires the solution of a three-region fields problem which is governed by Laplace's equation. The geometry of the problem is as shown in Figure A.3.

The Fourier component solutions of Laplace's equation in the three-regions of interest will take the form:

$$\begin{aligned}
&(a)\quad \hat{\Phi}_{n1} = A_{n1} \cosh k_n(y-d) + B_{n1} \sinh k_n(y-d) && 0 \leq y \leq d \\
&(b)\quad \hat{\Phi}_{n2} = A_{n2} \cosh k_n y + B_{n2} \sinh k_n y && -\delta \leq y \leq 0 \qquad (A.7) \\
&(c)\quad \hat{\Phi}_{n3} = A_{n3} \cosh k_n(y+\delta) + B_{n3} \sinh k_n(y+\delta) && -h \leq y \leq -\delta
\end{aligned}$$

where again the solution axes have been shifted to make calculations more efficient.

The six (6) boundary conditions required to evaluate the unknown constants of equation (A.7) are given as:

(a) $\hat{\Phi}_{n1}(y=d) = \hat{v}_n$

(b) $\varepsilon_p \nabla_y \hat{\Phi}_{n2}\Big)_{y=0} - \varepsilon_o \nabla_y \hat{\Phi}_{n1}\Big)_{y=0} = \hat{Q}$

(c) $\hat{\Phi}_{n1}(y=0) = \hat{\Phi}_{n2}(y=0)$

(d) $\hat{\Phi}_{n2}(y=-\delta) = \hat{\Phi}_{n3}(y=-\delta)$

Appendix A

Asymmetric Channel with Plexiglas Disk

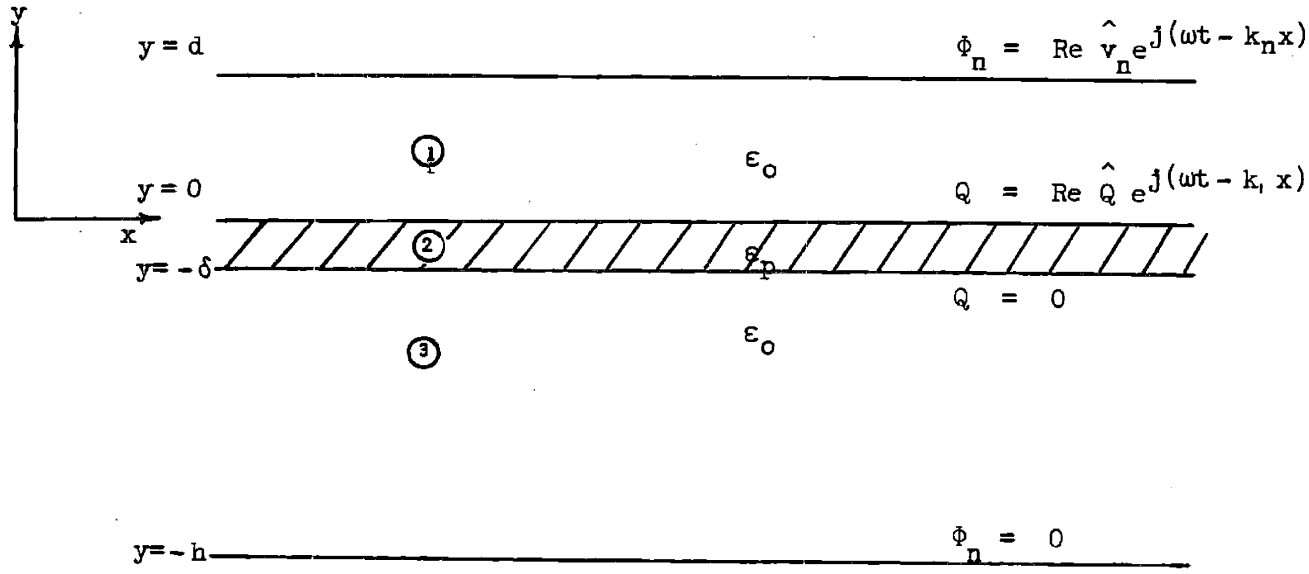

Figure A.3

Appendix A

(e) $\varepsilon_o \nabla_y \hat{\Phi}_{n3}\Big)_{y=-\delta} = \varepsilon_p \nabla_y \hat{\Phi}_{n2}\Big)_{y=-\delta}$

(f) $\hat{\Phi}_{n3}(y=-h) = 0$

Note that the displacement current density normal to the channel axis at the electrode interface is given by:

$$\hat{J}_n = -j\omega\varepsilon_o k_n B_{n1} \tag{A.9}$$

It is therefore only necessary to determine the unknown coefficient B_n in equation (A.7.a) using the boundary conditions of equation (A.8).

Determining B_{n1} and using it in equation (A.9) specifies the modified source $\hat{J}'_S$ and channel capacitance C'_{nC} terms for the physical arrangement of interest. These modified terms are:

$$C'_{nC} = \frac{\varepsilon_o k_n[\varepsilon_r f_1 + \tanh k_n d]}{[1+\varepsilon_r f_1 \tanh k_n d]} \quad \text{farads/m}^2 \tag{A.10}$$

and

$$\hat{J}'_S = \frac{j\omega\hat{Q}\,\delta_{-1n}}{\cosh k_n d[1+\varepsilon_r f_1 \tanh k_n d]} \quad \text{amps/m}^2 \tag{A.11}$$

where:

$$f_1 = \frac{1+\varepsilon_r \tanh(h-\delta)\tanh k_n\delta}{\varepsilon_r \tanh k_n(h-\delta) + \tanh k_n\delta} \tag{A.12}$$

These results combined with results of Chapter III provide the theory for the actual generator built for experimental measurements.

APPENDIX B

Experimental Generator:

General Generator Arrangement:

An asymmetrically loaded, charge-constrained synchronous generator was designed and built as part of this thesis project so as to provide verification of theoretical results. A sketch of the device built is presented in figure B.1.

The physical measurements of this generator are given below and should be used in any application of theory to predict output. Note that a mean wavelength, and therefore mean wavenumber, is used to characterize the load section. This is necessary since the wavelengths at the inside and outside tips of the load electrodes are different, due to the cylindrical geometry. Since the theory considers a rectangular channel this constitutes an approximation; however, the results as shown in Chapter IV indicate that it is a good one.

$$\bar{\lambda}_1 = 18.6 \times 10^{-2} \text{ m}$$

$$\bar{k}_1 = 33.8 \text{ m}^{-1}$$

$$\delta = .6 \times 10^{-2} \text{ m}$$

$$d = .5 \times 10^{-2} \text{ m}$$

$$(h - \delta) = 10.9 \times 10^{-2} \text{ m}$$

$$A_{electrode} = 11.5 \times 10^{-4} \text{ m}^2$$

$$a/c = .61$$

$$\omega_e = 60 \text{ cps}$$

$$\omega_m = 10 \text{ cps}$$

$$\varepsilon_r = 4.0$$

$$\varepsilon_o = 8.854 \times 10^{-12} \text{ farad/m}$$

Appendix B

Plexiglas was chosen as the material to be used for the structural support of the load electrodes because of its inherent attributes such as easy workability and transparency and its electrical properties are known. The plexiglas was chosen for the charge disk material principally for its extremely long characteristic relaxation time for bulk free charge. Charges placed on the disk by rotating it through the corona exciter section remain in place long enough to easily complete a full set of experimental measurements. The charge disk can be fully energized in less than 10 sec. and then the corona section may be turned off to eliminate noise in the electrode output signals.

In order that the corona exciting field would be in synchronism with the charge wave established on the disk, it was required that disk rotational frequency be divisible into the exciting voltage frequency an integer number of times. For the laboratory generator:

$$\frac{w_{electrical}}{w_{mechanical}} = \frac{60 \text{ HZ}}{10 \text{ cps}} = 6$$

This establishes six wavelengths of charge distribution around the periphery of the disk. The disk speed was obtained by using an 1800 rpm synchronous motor driving the shaft with a toothed, flexible belt and a set of 3:1 speed-reducing pulleys. With both the motor and corona being driven from the same electrical mains, the maintenance of synchronism was not a problem. Electrodes were arranged on the load disk at six electrodes per wavelength of charge distribution. Although there were six full wavelengths of charge distribution about the load section circumference, only

Appendix B

five wavelengths of load electrodes were installed. The sixth wavelength was left clear to accommodate the corona source.

Measurement of Disk Charge Density:

An important variable in describing the generator output is the magnitude of the charge distribution wave on the disk. It is not possible to gat an accurate measure of this charge magnitude simply by knowing the magnitude of the corona voltage. A direct measurement of the distribution was obtained using a Kuthly Electrometer model 610B in conjunction with a flat plate sensing proble of known area. The probe was mounted in the location where the corona source is set during the disk charging cycle. Manually rotating the disk then puts the probe under the influence of the charge, the magnitude being a function of position.

The electrometer is a dc instrument which measures the charge by integrating the current required to set up image charges for that charge influencing its probe. For this reason, it was necessary to make the rotation of the disk for charge distribution purposes extremely slow. Using this scheme for charge measurement gave consistent, reproduceable results which compared very well with theoretical predictions as shown in Table 4.1.

Pictures of the loading section with the electrodes loaded individually and in parallel are given in Figure B.2. These pictures also show the electrometer probe and corona source as they appear when mounted.

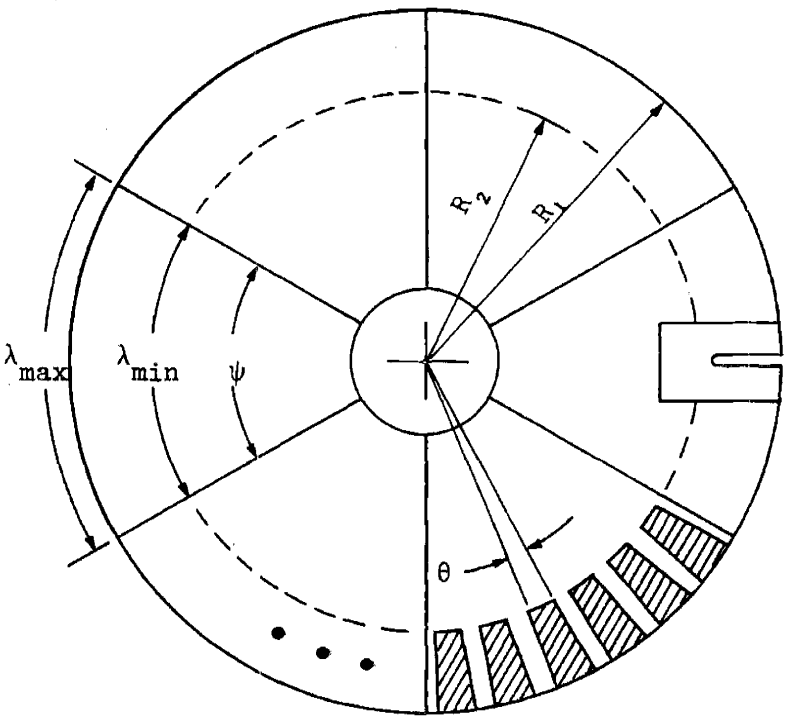

Load Disk

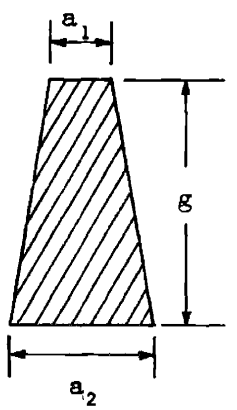

Electrode

$R_1 = 14.0 \times 10^{-2}$ m

$R_2 = 21.5 \times 10^{-2}$ m

$\psi = 60°$

$\theta = 6.1°$

$a_1 = 1.0 \times 10^{-2}$ m

$a_2 = 2.15 \times 10^{-2}$ m

$g = 7.5 \times 10^{-2}$ m

$\omega_m = \dfrac{\omega \text{ electrical}}{6}$

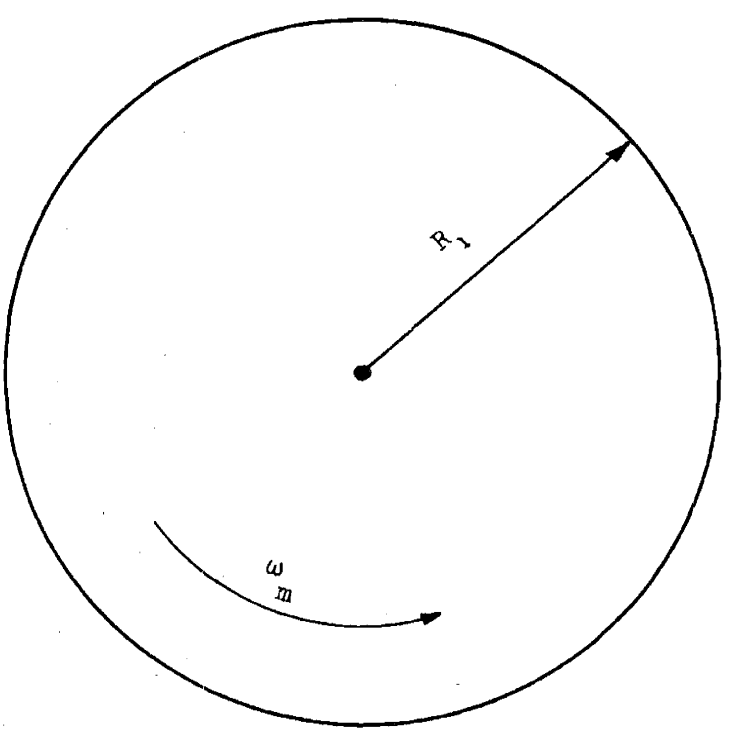

Charge Disk

Figure B.1

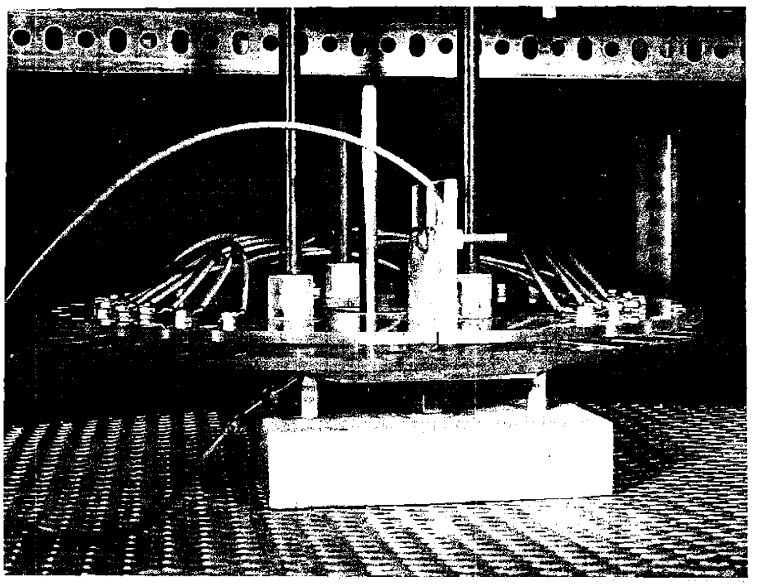

(a)

View Showing Load Electrodes of the Same Phase Connected in Parallel. Note Corona Source in Position in Foreground.

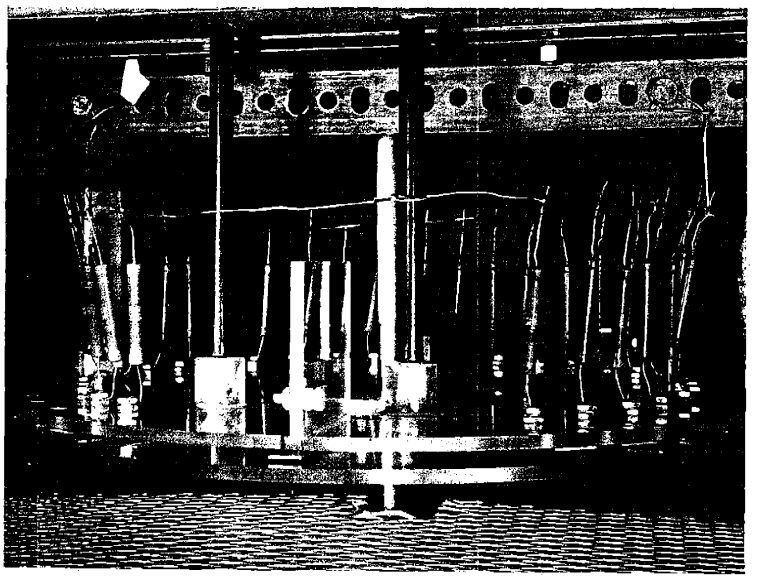

(b)

View Showing Each Electrode with Individual Resistive Loading. Note Electrometer Charge Measuring Probe in Position in Foreground.

Figure B.2

APPENDIX C

Computer Programs for Calculation:

The programs C.1 and C.2 can be used to calculate the capacitance ratio CAPR and power ratio POWR of Equations (3.39) and (3.41), respectively. These ratios provide a comparison between discretely loaded and continuous loaded, charge-constrained synchronous generators. If it is desired to calculate both of these ratios at the same time, the programs may be efficiently combined to decrease the computer time required.

The required inputs have, for the most part, been defined in Chapters I and II.

KD = $k_1 d$

KDELTA = $k_1 \Delta$

ALPHA = a/c

s = number of phases

The integer M sets the upper limit on the summation over n. This series converges rapidly and six contributing terms provide very good accuracy. Recall from Chapter IV that terms in this sum are contributed only for:

$$n = 1; \quad \frac{(n+1)}{s} = \text{integer}; \quad \frac{(n-1)}{s} = \text{integer}$$

The outputs are:

H = capacitance for continuous generator

F = total value of double sum over s and n

K = CAPR or POWR (depending on program being used)

Appendix C

```
JPOWR     MAD

START     PRINT COMMENTS TYPE KD, KDELTA, ALPHA, S, M, GO$
          INTEGER N,R,S,M
          READ DATA
          W'R GO .L.0.5, TRANSFER TO END
          PI = 3.14159
          KC = 2*PI/S
          G = 2.0/S
          H = TANH.(KD) + 1/TANH.(KDELTA)
          KA =  ALPHA*KC
          KB = (1.0 - ALPHA)*KC
          F =  0.0
          THROUGH SUM, FOR N= 1.0,1.0,N.G.M
          A = N*(TANH.(N*KD) + 1/TANH.(N*KDELTA))
          B = (SIN.(N*KA/2)*SIN.(N*KB/2)*SIN.(N*KC/2))/(N*N*N*KA*KB*KC/8)
          C = 0
          THROUGH RSUM, FOR R = 0, 1.0,R.GE.S
          D = COS.(2*PI*N*R/S)*COS.(2*PI*R/S)
RSUM      C = C+D
SUM       F = A*B*C*G + F
          K = H*ALPHA*SIN.(KA/2)*SIN.(KA/2)*4/(F*KA*KA)
          P'T V, H,F,K
          VECTOR VALUES V = $3E12.6*$
          T'O START
END       CONTINUE
          E'M
```

Program C.2

Appendix C

```
JCAPR      MAD

START      PRINT COMMENT$ TYPE KD, KDELTA, ALPHA, S,M,GO$
           INTEGER N,R,S,M
           READ DATA
           W'R GO .L.0.5, TRANSFER TO END
           PI = 3.14159
           KC = 2*PI/S
           G = 2.0/S
           H = TANH.(KD) + 1/RANH.(KDELTA)
           KA = ALPHA*KC
           KB = (1.0 - ALPHA)*KC
           F = 0.0
           THROUGH SUM, FOR N= 1.0,1.0,N.G.M
           A = N*(TANH.(N*KD) + 1/TANH.(N*KDELTA))
           B = (SIN.(N*KA/2)*SIN.(N*KB/2)*SIN.(N*KC/2))/(N*N*N*KA*KB*KC/8)
           C = 0
           THROUGH RSUM, FOR R=0,1.0,r.GE.S
           D = COS.(2*PI*N*R/S)*COS.(2*PI*R/S)
RSUM       C = C+D
SUM        F = A*B*C*G + F
           K = H/F
           P'T V, H,F,K
           VECTOR VALUES V = $3E12.6*$
           T'O START
END        CONTINUE
           E'M
R 1.033 + .283
```

Program C.1

LIST OF REFERENCES

1. Woodson, H. H., and Melcher, J.R., Electromechanical Dynamics, Chapter 7, (in publication, John Wiley & Sons, Inc., New York, N. Y.

2. Trump, J. G., "Electrostatic Sources of Electric Power", Electrical Engineering, June 1947.

3. Fitzgerald, A. E., and Kingsley, C. Jr., Electric Machinery, 2nd Ed. (1961), McGraw-Hill Inc., New York, N. Y., p. 83.

4. Marks, A., Barreto, E., and Chu, C. K., "Charged Aerosol Energy Converter", AIAA Journal 2, No. 1, January 1964.

5. Devitt, E. B., "Power Density on An AC Charged Particle Generator", Int. Memorandum No. 140, Continuum Electromechanics Grou, MIT, 1968

6. Kahn, C., and Gourdine, M. C., "Electrogasdynamic Power Generation", AIAA Journal 2, No. 8, August 1964, pp. 1423-1427

7. Zipkin, M. A., and Edwards, R. N. "Power Systems for Space Flight", Academic Press, New York, N.Y. 1963, p. 917, and "Electrostatic Power Generation for Space" by Coenraads, C., Denholm A. S., and Lovelle, J. E., and McCoy, F. J.

8. Van de Graaff, R. J., Trump, J. G., and Buechner, W. W. "Electrostatic Generators for the Acceleration of Charged Particles", Reports on Progress in Physics, Vol. XI, p. 1 (1948).

9. Gray, J. "Electrical Influence Machines", Whittaker and Co., London, England, 1890.

10. Reeve, W. F., "Traveling-Wave Synchronous Electrohydrodynamic Power Generation", S. M. Thesis, Dept. of Electrical Engineering, MIT, (1967).

11. Herold, L., "Traveling-Wave Charged Particle Generation", S. M. Thesis, Dept. of Electrical Engineering, MIT, (1967).

12. Melcher, J.R. "A Self-Excited Traveling-Wave Electrostatic and Electrohydrodynamic Generator", Int. Memorandum No. 135, Continuum Electromechanics Group, MIT, Dec. 1967

13. Regan, J. P., "A Cylindrical Charge-Constrained Synchronous Generator" Internal Memo. No. 134, Continuum Electromechanics Group, MIT, November 1967.